



Quadratic magnetic gradients from seven- and nine-spacecraft constellations

Chao Shen¹, Gang Zeng², Rungployphan Kieokaew³, and Yufei Zhou¹

¹School of Science, Harbin Institute of Technology, Shenzhen 518055, China

²School of Mathematics and Physics, Jingchu University of Technology, Jingmen, China

³Institut de Recherche en Astrophysique et Planétologie (IRAP), Toulouse, France

Correspondence: Chao Shen (shenchao@hit.edu.cn) and Gang Zeng (gzeng2014@126.com)

Received: 7 May 2024 – Discussion started: 17 May 2024

Revised: 28 November 2024 – Accepted: 29 November 2024 – Published: 30 January 2025

Abstract. To uncover the dynamics of magnetized plasma, it is crucial to determine the geometric structure of the magnetic field, which depends on its linear and quadratic spatial gradients. Estimating the linear magnetic gradient requires at least 4 simultaneous magnetic measurements, while calculating the quadratic gradients generally requires at least 10. This study focuses on deriving both linear and quadratic spatial gradients of the magnetic field using data from the nine-spacecraft (9S/C) HelioSwarm or seven-spacecraft (7S/C) Plasma Observatory constellations. Time series magnetic measurements, combined with transformations between reference frames, were employed to determine the apparent velocity of the magnetic structure and the quadratic magnetic gradient components along the direction of motion. The linear gradient and remaining components of the quadratic gradient were derived using the least-squares method with iterative calculations applied to ensure precision. The validity of the approach was demonstrated using magnetic flux ropes and dipole magnetic field models. The findings indicate that constellations with at least seven spacecraft in nonplanar configurations can successfully yield linear and quadratic spatial gradients of the magnetic field.

– Constellations containing at least seven spacecraft with nonplanar configurations are required for the approach.

1 Introduction

Multi-spacecraft constellations provide a unique capability to observe plasma processes at various spatiotemporal scales simultaneously. In particular, in situ magnetic measurements from such constellations enable the deduction of magnetic gradients, allowing for the investigation of fine magnetic structures, current densities, and magnetic field geometries. Typically, magnetic measurements from at least four spacecraft in a nonplanar configuration are required to deduce the three-dimensional (3-D) linear spatial gradient of a magnetic field (Harvey, 1998; Chanteur, 1998; Chanteur and Harvey, 1998; Shen et al., 2003; De Keyser et al., 2007; De Keyser, 2008; Hamrin et al., 2008; Shen et al., 2012). Additionally, linear spatial gradients of other scalar fields (e.g., plasma moments) or vector fields (e.g., an incompressible velocity field) can be obtained similarly. This is done by performing a Taylor expansion around the origin (e.g., the four-spacecraft mesocenter) up to the first order; the linear gradient, which provides a (unique) solution that fits the measurements, is then obtained using the least-squares method (Harvey, 1998; Chanteur, 1998; Chanteur and Harvey, 1998; Shen et al., 2003; Broeren et al., 2021).

The Cluster mission (Escoubet et al., 1997, 2001) and the Magnetospheric Multiscale (MMS; Burch et al., 2015) mission both utilize four-spacecraft constellations arranged in a tetrahedral configuration. Using the simultaneous magnetic measurements from these missions allows the linear spatial

Key points.

- An iterative algorithm for the quadratic magnetic gradient based on measurements with constellations comprising at least seven spacecraft is presented.
- Magnetic flux ropes and dipole magnetic field testing demonstrated the validity of the approach.

gradient of the magnetic field, e.g., the current density distribution, to be estimated and the topology of the magnetic field to be further derived (Dunlop et al., 2002b; Shen et al., 2003, 2008, 2012, 2014; Shi et al., 2005; Runov et al., 2006; Shi et al., 2010; Zhang et al., 2011; Rong et al., 2011; Burch and Phan, 2016; Dong et al., 2018; Pitout and Bogdanova, 2021; Haaland et al., 2021). Furthermore, four-point magnetic field measurements can also be applied to determine the orientation and motion of planar discontinuities (Russell et al., 1983; Dunlop et al., 2002a; Sonnerup et al., 2004) as well as the geometry of curved boundary layers (Kieokaew et al., 2018; Kieokaew and Foullon, 2019; Shen et al., 2020). For a planar constellation or a constellation comprising three spacecraft, only a 2-D linear magnetic gradient in the constellation plane can generally be derived (Vogt et al., 2009, 2013; Shen et al., 2012). Nevertheless, for certain structures, such as 1-D and force-free structures, magnetic measurements from planar constellations or even double-star constellations can also be reduced to a 3-D linear magnetic gradient (Vogt et al., 2009, 2013; Shen et al., 2012).

To estimate second spatial derivatives of the magnetic field (or Hessian matrix over each component of the magnetic field), simultaneous magnetic measurements from a constellation with more spacecraft are required. Considering a Taylor expansion of the magnetic field around the origin up to the second order, there are 10 unknown parameters: one magnetic measurement at the origin, three components of the linear magnetic gradient, and six components of the second-order magnetic gradient (i.e., the quadratic gradient tensor is symmetric). To obtain a unique solution to the system of equations, we need a number of unknown parameters to be equal to, or less than, the number of the constraints (i.e., equations). Therefore, 10-point measurements are required to solve the quadratic gradient (Chanteur, 1998; Shen et al., 2021b) given that not all spacecraft are simultaneously on the same quadratic surface (Zhou and Shen, 2024). Nevertheless, the quadratic gradient of a magnetic field can still be estimated from four-spacecraft constellations if additional current density measurements deduced from electron and ion measurements and certain physical constraints, such as Ampère's law and magnetic Gauss's law, are utilized (Liu et al., 2019; Torbert et al., 2020; Denton et al., 2020; Shen et al., 2021a). Utilizing the linear and quadratic gradients of the magnetic field means that the complete geometry of a magnetic field, which concerns linear, e.g., current sheets, and nonlinear spatial structures, e.g., magnetic flux ropes, can be determined (Shen et al., 2021a). Furthermore, the calculation of quadratic spatial gradients of physical electromagnetic and plasma quantities in general allows us to study nonlinear plasma dynamics involving second-order spatial derivatives, such as in plasma turbulence (e.g., Politano and Pouquet, 1998a, b; Yang, 2019; Pecora et al., 2023) and nonlinear wave dynamics (e.g., Chian et al., 1998, 2022), among others.

The HelioSwarm mission (Klein et al., 2023) is a nine-spacecraft (9S/C) constellation consisting of one hub and eight nodes planned to be launched in 2029 by the National Aeronautics and Space Administration (NASA). The swarm of nine spacecraft will allow simultaneous cross-scale observations of turbulent solar-wind plasmas for the first time in the vicinity of Earth. Specifically, each spacecraft of HelioSwarm will be equipped with a fluxgate magnetometer and a search coil magnetometer, allowing comprehensive measurements of magnetic fields at nine points simultaneously. The Plasma Observatory (Retinò et al., 2022) is a new European Space Agency (ESA) mission with a seven-spacecraft (7S/C) constellation in the solar-terrestrial environment, currently under Phase-A study. One important topic for these two new multi-spacecraft constellations is to ascertain how the linear and quadratic gradients of the magnetic field can be inferred from seven- or nine-point magnetic measurements, allowing the fine, nonlinear spatial structures of the magnetic field in a space plasma to be identified. In this study, a new algorithm for calculating the linear and quadratic spatial gradients of the magnetic field from seven- or nine-point simultaneous magnetic measurements was derived using the least-squares method. By considering the transformation of the reference frame involving mixed space-time derivatives of the magnetic field, we demonstrate that seven- or nine-point simultaneous measurements can be used to estimate quadratic spatial gradients. Here, by exploiting the least-squares method, we propose an iterative approach to achieve an optimal solution.

The remainder of this paper is organized as follows. The new algorithm for calculating the linear and quadratic magnetic gradients from seven- or nine-point simultaneous magnetic measurements is presented in Sect. 2; a description of the tests conducted for two typical nonlinear magnetic structures (a cylindrical force-free flux rope and a dipole magnetic field) which were utilized to check the validity and accuracy of the new algorithm is given in Sect. 3; the accuracy of the algorithm is evaluated in Sect. 4; and finally, the conclusions are presented in Sect. 5.

2 Methodology

2.1 The scheme

Calculation of the linear and quadratic gradients of a magnetic field generally requires simultaneous magnetic measurements from at least 10 spacecraft. There are $3 + 9 + 18 = 30$ parameters in the Taylor expansion up to the second order, and $3N$ magnetic field measurements in an array with N spacecraft are needed accordingly. Thus, using the magnetic measurements of the nine-spacecraft (9S/C) HelioSwarm or seven-spacecraft (7S/C) Plasma Observatory constellation means that additional constraints are required. The transfer relationships between different reference frames

are the proper limitations used for completely determining the spatial linear and quadratic gradients of the magnetic field. In these limits, we assume that the magnetic structures are slowly evolving during their passages through the multi-point constellations such that any differences in the measurements at different spacecraft can be attributed to the spatial variations rather than the temporal changes (i.e., evolution of magnetic structures).

The Taylor expansion of the magnetic field within two orders is expressed using

$$\mathbf{B}(t, \mathbf{r}) = \mathbf{B}(t, \mathbf{r}_c) + (\mathbf{r} - \mathbf{r}_c) \cdot \nabla \mathbf{B}(t, \mathbf{r}_c) + \frac{1}{2}(\mathbf{r} - \mathbf{r}_c)(\mathbf{r} - \mathbf{r}_c) \cdot \nabla \nabla \mathbf{B}(t, \mathbf{r}_c). \quad (1)$$

The Taylor expansion of each component of the magnetic field at each spacecraft α can be written as

$$f_{(\alpha)} = f_c + x_{(\alpha)}^i (\nabla_i f)_c + \frac{1}{2} x_{(\alpha)}^i x_{(\alpha)}^j (\nabla_i \nabla_j f)_c = f_c + x_{(\alpha)}^i g_i + \frac{1}{2} x_{(\alpha)}^i x_{(\alpha)}^j G_{ij}, \quad (2)$$

where f represents any one of the three components, B^1 , B^2 , or B^3 , of the magnetic field, \mathbf{B} . The first-order gradient is denoted as $g_i \equiv (\nabla_i f)_c$, where $i = 1, 2, 3$, i.e., the three Cartesian components, and the second-order gradient is denoted as $G_{ij} \equiv (\nabla_i \nabla_j f)_c$, where $i, j = 1, 2, 3$.

Conventionally, 10-point simultaneous measurements are necessary to infer both the first-order and the second-order spatial gradients of a physical scalar field (Chanteur, 1998; Shen et al., 2021b). To obtain such spatial gradients with the 9S/C HelioSwarm and 7S/C Plasma Observatory, we consider adding additional physical constraints to the system of equations. Figure 1 shows a schematic diagram of observation of a magnetic structure by the Plasma Observatory constellation. The shape of the constellation is ideal but this does not change the generality and applicability of our method.

The following transformation relationship involving the mixed space–time derivatives is used for the magnetic measurements:

$$\partial_t \mathbf{B} = -\mathbf{V} \cdot \nabla \mathbf{B} \text{ and } \partial_t \nabla \mathbf{B} = -\mathbf{V} \cdot \nabla \nabla \mathbf{B}. \quad (3)$$

By computing the temporal derivative, $\partial_t \mathbf{B}$, and then the temporal derivative of spatial gradient $\partial_t \nabla \mathbf{B}$, this relationship allows both the apparent velocity, \mathbf{V} , of the magnetic structure and the nine components of the quadratic magnetic gradient tensor along the direction of motion, $\hat{\mathbf{V}} \cdot \nabla \nabla \mathbf{B}$, to be obtained (Shen et al., 2021a). The constraints to Eq. (3) are that the plasmas are highly conductive and have a very low velocity ($\mathbf{V}/c \ll 1$, where \mathbf{V} is the apparent speed of the magnetic structure and c is the speed of light in a vacuum) and that the physical processes are slowly evolving at low frequencies. The truncation errors in Eq. (3) are on the order of \mathbf{V}/c .

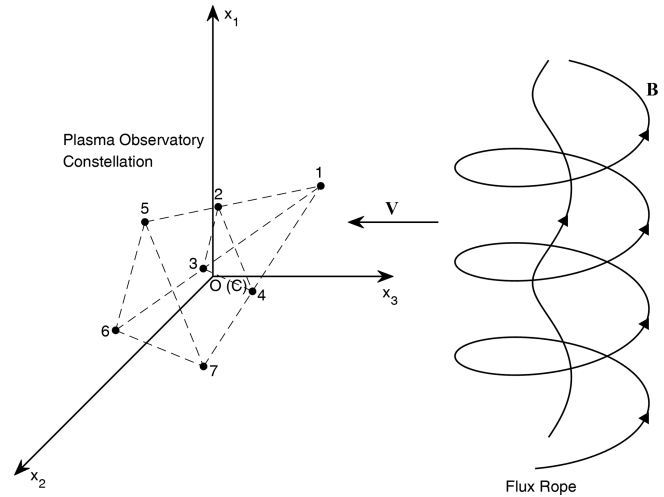


Figure 1. Schematic plot showing observation of a magnetic structure by the Plasma Observatory constellation, which is composed of seven spacecraft. (The special configuration is similar to the mission term proposal, and the actual geometry can deviate from it.) Barycentric coordinates are adopted; thus, the center C of the constellation overlaps with the origin, O, of the Cartesian coordinates (x_1, x_2, x_3), the magnetic structure is assumed to be moving at velocity \mathbf{V} relative to the constellation, and the x_3 axis is presumed to be anti-parallel to \mathbf{V} .

2.1.1 The zeroth iteration

First, the temporal variation rate $\partial_t \mathbf{B}$ and first-order magnetic gradient $(\nabla \mathbf{B})^{(0)}$, where the uppercase label (0) denotes the zeroth order, can be obtained from seven- or nine-point simultaneous magnetic measurements. Here, the change rate of the magnetic field can be obtained from the temporal (time series) measurements at each spacecraft. The linear spatial gradient can be obtained using four-spacecraft techniques (Chanteur, 1998; Harvey, 1998; Shen et al., 2003). Using Eq. (3), we can thus obtain the apparent velocity, \mathbf{V} , of the magnetic structure (Shen et al., 2021a). Next, the longitudinal components of the second-order magnetic gradient, $\hat{\mathbf{V}} \cdot \nabla \nabla \mathbf{B} = \frac{1}{V} \partial_3 \nabla \mathbf{B}$, can be deduced from the transformation relationship (Eq. 3). These steps are described in detail in Sect. 2.2.1. Finally, the remaining nine components of the second-order magnetic gradient (i.e., the transverse component, $G_{rs}^{(1)} = (\nabla_r \nabla_s f)^{(1)}$, where $r, s = 1, 2$) can be determined from the seven- or nine-point simultaneous magnetic measurements using the least-squares method, allowing for a first-order quadratic magnetic gradient, $(\nabla \nabla \mathbf{B})^{(1)}$, to be obtained, as described next.

2.1.2 The first-order iteration

Provided with the first-order quadratic magnetic gradient, $(\nabla \nabla \mathbf{B})^{(1)}$, the corrected first-order linear magnetic gradient, $(\nabla \mathbf{B})^{(1)}$, can be found using the least-squares method. Furthermore, the corrected apparent velocity, $\mathbf{V}^{(1)}$, of the

magnetic structure and the longitudinal components of the second-order quadratic magnetic gradient, $(\hat{\mathbf{V}} \cdot \nabla \nabla \mathbf{B})^{(2)}$, can be obtained from the transformation relationship (Eq. 3). Again, the corrected transverse components of the quadratic magnetic gradient ($G_{rs}^{(2)}, r, s = 1, 2$) are obtained using the least-squares method, allowing a second-order quadratic magnetic gradient $(\nabla \nabla \mathbf{B})^{(2)}$ to be obtained.

The iterations are performed repeatedly until results converge, which means satisfactory results have been achieved.

For the 7S/C Plasma Observatory, the seven-point magnetic measurements in 3-D yield $7 \times 3 = 21$ independent parameters, while the reference frame transformation provides nine constraints, resulting in $21 + 9 = 30$ input parameters in total. The objective is to determine the magnetic field (3 parameters), first-order gradient (9 parameters), and quadratic magnetic gradient (18 parameters) at the mesocenter of the constellation, a total of $3 + 9 + 18 = 30$ parameters. Therefore, this scheme is reasonable and such that the solution to the system of equations can be uniquely determined.

Clearly, the 9S/C magnetic measurements of HelioSwarm are sufficient to draw first-order and quadratic magnetic gradients using this method. These results indicate that the developed method is suitable for constellations comprising at least seven spacecraft.

2.2 Practical steps of the algorithm

Details of the steps used are given below.

2.2.1 The zeroth iteration

We first assume a linear approximation in space and let $G_{ij}^{(0)} = 0$. The magnetic field, $\mathbf{B}_c^{(0)}$, and its linear gradient, $(\nabla \mathbf{B})^{(0)}$, at the mesocenter of the constellation can then be obtained using the following formulas (Harvey, 1998; Shen et al., 2003):

$$\mathbf{B}_{ci}^{(0)} = \frac{1}{N} \sum_{\alpha=1}^N B_{\alpha i}, \tag{4}$$

$$(\partial_i B_j)_c^{(0)} = \frac{1}{N} \sum_{\alpha=1}^N B_{\alpha i} r_{\alpha k} R_{kj}^{-1}, \tag{5}$$

where the volume tensor is $R_{kj} = \frac{1}{N} \sum_{\alpha=1}^N r_{\alpha k} r_{\alpha j}$ or $\mathbf{R} \equiv$

$\frac{1}{N} \sum_{\alpha=1}^N \mathbf{r}_{\alpha} \mathbf{r}_{\alpha}$, where N is the number of spacecraft within

the constellation and R_{kj}^{-1} is the inverse of the volume tensor R_{kj} . The determinant of the volume tensor is required to be nonzero, i.e., $R = \det(\mathbf{R}_{kj}) \neq 0$. This is equivalent to the constellation being nonplanar (i.e., not all spacecraft are on the same plane).

The temporal variation rate, $(\partial_t \mathbf{B})_c^{(0)}$, is readily obtained from central differences in the magnetic observation time series. Now the frame transformation relationship, Eq. (3), is

reduced to the apparent velocity, $\mathbf{V}^{(0)}$, of the magnetic structure and the longitudinal components of the quadratic magnetic gradient $(\partial_3 \nabla \mathbf{B})^{(1)}$.

First, the zeroth approximation of the apparent velocity of the magnetic structure $\mathbf{V}^{(0)}$ can be found using the frame transformation relationship:

$$(\partial_t \mathbf{B})^{(0)} = -\mathbf{V}^{(0)} \cdot (\nabla \mathbf{B})^{(0)}. \tag{6}$$

Then, using the relationship

$$\partial_t (\nabla \mathbf{B})^{(0)} = -\mathbf{V}^{(0)} \cdot (\nabla \nabla \mathbf{B})^{(1)}, \tag{7}$$

the longitude component of the quadratic magnetic gradient at the first order can be derived as follows:

$$(\partial_3 \nabla \mathbf{B})_c^{(1)} = \frac{1}{V^{(0)}} \partial_t (\nabla \mathbf{B}(t, \mathbf{r}_c))^{(0)}, \tag{8}$$

which is just $(G_{31}^{(1)}, G_{32}^{(1)}, G_{33}^{(1)})$.

The remaining components of the quadratic magnetic gradients can be deduced using the least-squares method.

We assume that the following applies:

$$S = \frac{1}{N} \sum_{\alpha=1}^N \left[f_c^{(0)} + x_{(\alpha)}^i g_i^{(0)} + \frac{1}{2} x_{(\alpha)}^i x_{(\alpha)}^j G_{ij}^{(1)} - f_{(\alpha)} \right]^2, \tag{9}$$

which can also be written as

$$S = \frac{1}{N} \sum_{\alpha=1}^N \left[f_c^{(0)} + x_{(\alpha)}^i g_i^{(0)} - f_{(\alpha)} + \left(1 - \frac{1}{2} \delta_{i3} \right) x_{(\alpha)}^i x_{(\alpha)}^3 G_{i3}^{(1)} + \frac{1}{2} x_{(\alpha)}^p x_{(\alpha)}^q G_{pq}^{(1)} \right]^2. \tag{10}$$

where $p, q = 1, 2$.

If $\delta S = 0$, then

$$\frac{\partial S}{\partial G_{pq}} = \frac{1}{N} \sum_{\alpha=1}^N 2 \left[f_c^{(0)} + x_{(\alpha)}^i g_i^{(0)} - f_{(\alpha)} + \left(1 - \frac{1}{2} \delta_{i3} \right) x_{(\alpha)}^i x_{(\alpha)}^3 G_{i3}^{(1)} + \frac{1}{2} x_{(\alpha)}^r x_{(\alpha)}^s G_{rs}^{(1)} \right] \cdot x_{(\alpha)}^p x_{(\alpha)}^q = 0, \tag{11}$$

which reduces to

$$f_c^{(0)} \sum_{\alpha=1}^N x_{(\alpha)}^p x_{(\alpha)}^q + \sum_{\alpha=1}^N x_{(\alpha)}^i x_{(\alpha)}^p x_{(\alpha)}^q g_i^{(0)} - \sum_{\alpha=1}^N f_{(\alpha)} x_{(\alpha)}^p x_{(\alpha)}^q + \sum_{\alpha=1}^N \left(1 - \frac{1}{2} \delta_{i3} \right) x_{(\alpha)}^i x_{(\alpha)}^3 x_{(\alpha)}^p x_{(\alpha)}^q G_{i3}^{(1)} + \frac{1}{2} \sum_{\alpha=1}^N x_{(\alpha)}^r x_{(\alpha)}^s x_{(\alpha)}^p x_{(\alpha)}^q G_{rs}^{(1)} = 0, \tag{12}$$

resulting in $G_{rs}^{(1)} (r, s = 1, 2)$, i.e., $(G_{21}^{(1)}, G_{22}^{(1)}, G_{11}^{(1)})$. The constellation must be nonplanar to achieve this result. This is verified as follows.

Following Zhou and Shen (2024), in order for the solution to exist, it is expected that the position of all the spacecraft in the constellation must not obey the following formula:

$$a_{11} \left(x_{(\alpha)}^1 \right)^2 + a_{12} x_{(\alpha)}^1 x_{(\alpha)}^2 + a_{12} x_{(\alpha)}^2 x_{(\alpha)}^1 + a_{22} \left(x_{(\alpha)}^2 \right)^2 = 0, \tag{13}$$

where $a_{rs} (r, s = 1, 2)$ is a set of fixed coefficients. The above equations can be rewritten as follows:

$$a_{11} \left(x_{(\alpha)}^1 / x_{(\alpha)}^2 \right)^2 + 2a_{12} \left(x_{(\alpha)}^1 / x_{(\alpha)}^2 \right) + a_{22} = 0, \tag{14}$$

which reduces to $x_{(\alpha)}^1 / x_{(\alpha)}^2 = \text{constant}$. It means that all the spacecraft are in the plane parallel to the x_3 axis or the motion direction. Therefore, it is necessary to have the constellation not be planar in order to deduce the quadratic magnetic gradients as well as the linear magnetic gradient. The next iterations would also require this condition.

2.2.2 First-order iteration

Assuming that

$$S = \frac{1}{N} \sum_{\alpha=1}^N \left[f_c^{(1)} + x_{(\alpha)}^i g_i^{(1)} + \frac{1}{2} x_{(\alpha)}^i x_{(\alpha)}^j G_{ij}^{(1)} - f_{(\alpha)} \right]^2, \tag{15}$$

if $\delta S = 0$, then

$$\frac{\partial S}{\partial f_c^{(1)}} = 0, \quad \frac{\partial S}{\partial g_i^{(1)}} = 0. \tag{16}$$

From $\frac{\partial S}{\partial f_c^{(1)}} = 0$, it can be assumed that

$$\frac{1}{N} \sum_{\alpha=1}^N \left[f_c^{(1)} + x_{(\alpha)}^i g_i^{(1)} + \frac{1}{2} x_{(\alpha)}^i x_{(\alpha)}^j G_{ij}^{(1)} - f_{(\alpha)} \right] = 0, \tag{17}$$

meaning that

$$\begin{aligned} f_c^{(1)} &= \frac{1}{N} \sum_{\alpha=1}^N f_{(\alpha)} - \frac{1}{2N} \sum_{\alpha=1}^N x_{(\alpha)}^i x_{(\alpha)}^j G_{ij}^{(1)} \\ &= \frac{1}{N} \sum_{\alpha=1}^N f_{(\alpha)} - \frac{1}{2} R^{ij} G_{ij}^{(1)}. \end{aligned} \tag{18}$$

If $\frac{\partial S}{\partial g_i^{(1)}} = 0$, this can be reduced to

$$\begin{aligned} \frac{1}{N} \sum_{\alpha=1}^N \left[f_c^{(1)} + x_{(\alpha)}^i g_i^{(1)} + \frac{1}{2} x_{(\alpha)}^i x_{(\alpha)}^j G_{ij}^{(1)} - f_{(\alpha)} \right] x_{(\alpha)}^k &= 0, \end{aligned} \tag{19}$$

i.e., the following applies:

$$\begin{aligned} \frac{1}{N} \sum_{\alpha=1}^N x_{(\alpha)}^k x_{(\alpha)}^i g_i^{(1)} + \frac{1}{2} \frac{1}{N} \sum_{\alpha=1}^N x_{(\alpha)}^k x_{(\alpha)}^i x_{(\alpha)}^j G_{ij}^{(1)} - \frac{1}{N} \sum_{\alpha=1}^N f_{(\alpha)} x_{(\alpha)}^k &= 0. \end{aligned} \tag{20}$$

The tensor $R^{kij} = \frac{1}{N} \sum_{\alpha=1}^N x_{(\alpha)}^k x_{(\alpha)}^i x_{(\alpha)}^j$ is then defined, resulting in

$$R^{ki} g_i^{(1)} + \frac{1}{2} R^{kij} G_{ij}^{(1)} - \frac{1}{N} \sum_{\alpha=1}^N f_{(\alpha)} x_{(\alpha)}^k = 0. \tag{21}$$

Therefore, the first magnetic gradient is

$$\begin{aligned} g_{\ell}^{(1)} &= -\frac{1}{2} \left(R^{-1} \right)^{k\ell} R^{kij} G_{ij}^{(1)} \\ &\quad + \left(R^{-1} \right)^{k\ell} \cdot \frac{1}{N} \sum_{\alpha=1}^N f_{(\alpha)} x_{(\alpha)}^k. \end{aligned} \tag{22}$$

Using Eq. (3), it is now possible to obtain the corrected apparent velocity $\mathbf{V}^{(1)}$ of the magnetic structure and the longitudinal components of the corrected quadratic magnetic gradient $(\partial_3 \nabla \mathbf{B})^{(2)} ((\partial_3 \partial_i \mathbf{B})^{(2)})$ as in the zeroth iteration.

The least-squares method is then used to obtain the remaining nine components of the corrected quadratic magnetic gradient.

If

$$\begin{aligned} S &= \frac{1}{N} \sum_{\alpha=1}^N \left[f_c^{(1)} + x_{(\alpha)}^i g_i^{(1)} + \frac{1}{2} x_{(\alpha)}^i x_{(\alpha)}^j G_{ij}^{(2)} - f_{(\alpha)} \right]^2 \\ &= \frac{1}{N} \sum_{\alpha=1}^N \left[f_c^{(1)} + x_{(\alpha)}^i g_i^{(1)} - f_{(\alpha)} \right. \\ &\quad \left. + \left(1 - \frac{1}{2} \delta_{i3} \right) x_{(\alpha)}^i x_{(\alpha)}^3 G_{i3}^{(2)} + \frac{1}{2} x_{(\alpha)}^p x_{(\alpha)}^q G_{pq}^{(2)} \right]^2, \end{aligned} \tag{23}$$

then $G_{pq}^{(2)} (p, q = 1, 2)$ can be obtained using the same procedure as that used for the zeroth iteration so that all the components of the corrected quadratic magnetic gradient $(\nabla \nabla \mathbf{B})^{(2)}$ are obtained.

Similarly, two or more iterations can be performed until stable linear and second-order magnetic gradients are obtained.

This algorithm requires that the constellation be composed of at least seven spacecraft and that its configuration be nonplanar. Because both the 9S/C HelioSwarm and 7S/C Plasma Observatory satisfy these requirements, the linear and quadratic magnetic gradients can be readily obtained.

The curlometer technique (Dunlop et al., 2002b) is used to calculate the current density based on multiple spacecraft magnetic measurements, with the relative error estimated by

Table 1. Coordinates of the seven spacecraft in the barycenter coordinate system, with α denoting the spacecraft number.

α	$x_{(\alpha)} (R_E)$	$y_{(\alpha)} (R_E)$	$z_{(\alpha)} (R_E)$
1	0.0105	0.0016	0.0100
2	0.0135	0.0153	-0.0119
3	-0.0124	0.0155	-0.0026
4	0.0138	-0.0114	0.0139
5	0.0044	0.0157	0.0097
6	-0.0134	0.0152	0.0153
7	-0.0074	-0.0005	0.0052

the ratio between the divergence and the curl of the magnetic field, i.e., $\left| \frac{\nabla \cdot \mathbf{B}}{\nabla \times \mathbf{B}} \right|$. If the length and the magnetic field are normalized by the characteristic distance and magnetic strength (D, B_0), the equation becomes $\left| \frac{\nabla \cdot \mathbf{B}}{\nabla \times \mathbf{B}} \right| \approx \left| \frac{\nabla \cdot \mathbf{B}}{1} \right| = \left| \nabla \cdot \mathbf{B} \right|$. Therefore, the dimensionless divergence of the magnetic field calculated with observation data can be regarded as a reasonable measure of the relative error within the linear magnetic gradient. Similarly, the dimensionless $\left| \nabla(\nabla \cdot \mathbf{B})_c \right|$ can be used as a measure that describes the relative error in the quadratic magnetic gradient derived using the method.

3 Comparison of new method with analytical modeling

In this section, the new method is applied to two analytical magnetic field models (a cylindrical force-free flux rope and a dipole magnetic field) to evaluate their validity and accuracy. The applicability of this approach was tested on the 7S/C Plasma Observatory ($N = 7$) under the assumption that the seven-spacecraft cluster crosses a magnetic field structure (as illustrated in Fig. 1) by comparing the linear and quadratic gradients of the magnetic field obtained by the new method with those obtained by accurate modeling.

The positions of the seven spacecrafts in the barycentric coordinate system were generated randomly with Cartesian coordinates between -0.02 and $0.02 R_E$, as seen in Table 1. The 7S/C array is illustrated in Fig. 2.

The characteristic configuration of the spacecraft is described using several parameters. The three eigenvalues of the volumetric tensor R^{ij} are represented by w_1, w_2 , and w_3 (where $w_1 \geq w_2 \geq w_3$) (Harvey, 1998), with their square roots representing the characteristic half-widths of the S/C in the three orthogonal directions along the corresponding eigenvectors (Harvey, 1998). The characteristic size of the S/C constellation is twice the square root of the maximum eigenvalue, $L = 2\sqrt{w_1}$ (Robert et al., 1998; Shen et al., 2012). For the 7S/C constellation tested in this section, the three eigenvalues are $w_1 = 0.1643 \times 10^{-3} R_E^2$, $w_2 = 0.1104 \times 10^{-3} R_E^2$, and $w_3 = 0.0341 \times 10^{-3} R_E^2$. The characteristic size is $L = 2\sqrt{w_1} = 0.0256 R_E = 163.33$ km.

3.1 Flux rope

The flux rope was assumed to be force-free and cylindrically symmetrical. The magnetic field of the flux rope can be described using the Helmholtz equation, for which Lundquist (1950) provided analytical solutions in terms of the Bessel functions.

$$B_r = 0, \quad B_\phi(r) = B_0 J_1(\alpha r), \quad B_z(r) = B_0 J_0(\alpha r), \quad (24)$$

where r is the radial distance from the centric axis; α is a constant, with $1/\alpha$ representing the characteristic scale of the flux rope; B_0 is the peak axial field intensity; and J_0 and J_1 are the zeroth- and first-order Bessel functions of the first kind, respectively. For this test, we set $B_0 = 60$ nT and $\alpha = 1/R_E$.

The 7S/C array was assumed to cross the flux rope in a straight line at uniform velocity. The array is represented by the barycenter with the red dot in Fig. 3 and moves from $(-2, 0, 0) R_E$ to $(2, 0, 0) R_E$ along the x axis over a time interval of 100 s. The resolution of the magnetic field measurement was set to 1 s for the time series observations, and the characteristic size of the 7S/C array was set to $L = 0.0256 R_E$ for the gradients of the magnetic field at the barycenter along the trajectory to be obtained.

The linear gradient of the magnetic field ($\nabla_i B_k$) has 9 components, while the quadratic gradient ($\nabla_i \nabla_j B_k$) comprises 27 components. According to the analytical flux-rope model and symmetry of the quadratic gradients, only five independent components of the quadratic gradients $\nabla_1 \nabla_2 B_1$, $\nabla_1 \nabla_1 B_2$, $\nabla_2 \nabla_2 B_2$, $\nabla_1 \nabla_1 B_3$, and $\nabla_2 \nabla_2 B_3$ and three components of the linear gradient, $\nabla_2 B_1$, $\nabla_1 B_2$, and $\nabla_1 B_3$, are nonzero points on the x axis when using Cartesian coordinates, simplifying the comparison between the gradients derived from the proposed method and the analytical model.

The impact of iteration on the results was investigated first, with the results at two different points used to demonstrate the variation in the relative errors under iteration, as illustrated in Fig. 4. The relative error is defined as $\left| (X_{\text{algorithm}} - X_{\text{accurate}}) / X_{\text{accurate}} \right| \times 100\%$, where $X_{\text{algorithm}}$ and X_{accurate} represent the algorithm gradients derived using the new method and accurate values from the analytical model at the barycenter, respectively. As shown in Fig. 4a and c, the linear gradients converged to certain values within 50 iterations, and the final relative errors were lower than 0.02%. Figure 4b and d also indicate that the quadratic gradients converge. However, some quadratic gradients converged faster than others with fewer relative errors, and final relative errors of no more than 1.5% were obtained after 100 iterations. The maximum number of iterations was set to 100; thus, the gradients could be derived with good accuracy.

Figure 5 shows a comparison of the nonzero linear and quadratic gradients at the barycenter derived from our method with those derived from the analytical model. The algorithm gradients are consistent with the accurate gradients,

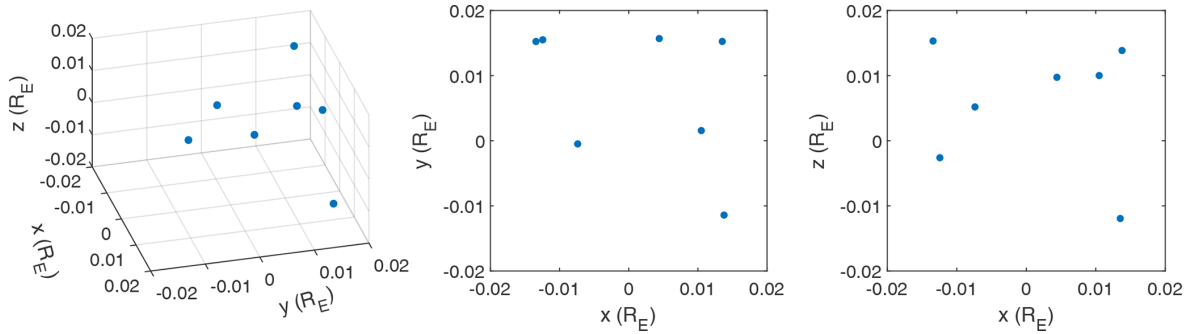


Figure 2. Configuration of the 7S/C constellation.

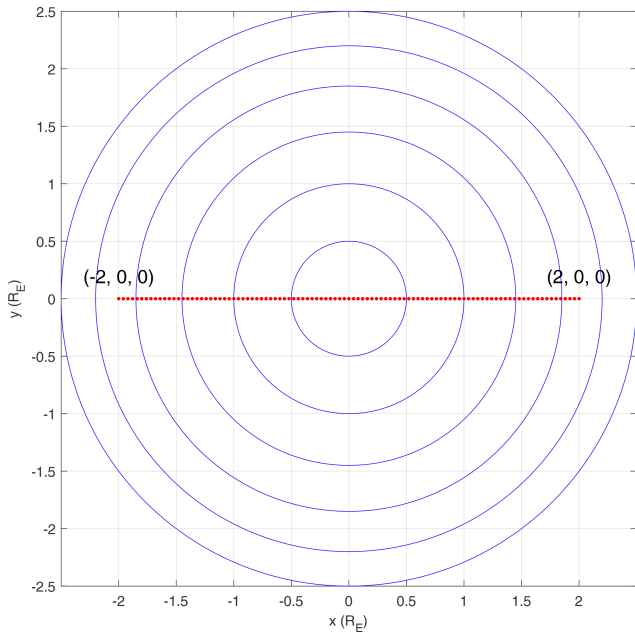


Figure 3. The cylindrical force-free flux-rope crossing by the 7S/C constellation as viewed from the axial direction. The trajectory of the barycenter of the constellation from $(-2, 0, 0) R_E$ to $(2, 0, 0) R_E$ over 100 s is shown by the dotted red line. The blue lines represent magnetic field lines.

indicating that the proposed method is effective and precise when used with flux ropes.

The relative errors in the gradients at points along the trajectory are shown in Fig. 6. All the relative errors in the linear gradients were lower than 0.1 %, and the vast majority of the relative errors for the quadratic gradients did not exceed 5 %. It should be noted that the barycenter is at $(0, 0, 0)$ at 50 s and that the nonzero components of the linear and quadratic gradients do not exist at $(0, 0, 0)$. The barycenter is at $(-0.04, 0, 0) R_E$ at 49 s, when accurate modeling and algorithm values for the quadratic gradient $\nabla_2 \nabla_2 B_2$ are 0.3 and $0.1570 \text{ nT } R_E^{-2}$, respectively. The relative error approaches 50%; however, the absolute error is just $0.143 \text{ nT } R_E^{-2}$, which

is approaching zero. Symmetrically, the situation described is the same as it would be if the barycenter were at $(0.04, 0, 0)$.

3.2 Dipole field

The proposed method was also tested and verified using a magnetic dipole field. The geomagnetic dipole field is mathematically expressed as

$$\begin{cases} B_x = -\frac{3xz}{r^5} B_0 \\ B_y = -\frac{3yz}{r^5} B_0 \\ B_z = \frac{r^2 - 3z^2}{r^5} B_0 \end{cases}, \quad (25)$$

where B_0 is the magnetic field at the Earth’s Equator and is defined by $B_0 = \frac{\mu_0 M}{4\pi R_E^3} = 30008 \text{ nT}$; $M = 7.76 \times 10^{22} \text{ A m}^2$ is the geomagnetic moment, with its direction set anti-parallel to the z axis; $x, y,$ and z are the coordinates of the field points measured by R_E ; and $r = \sqrt{x^2 + y^2 + z^2}$ is the radial distance from the origin measured by R_E .

The 7S/C array was assumed to cross the dipole field in a straight line at constant velocity, with the barycenter parallel to the x axis and moving from $(-5, 0, 5) R_E$ to $(5, 0, 5) R_E$ over 125 s, as illustrated in Fig. 7. The resolution of the magnetic field measurement was set to 1 s, and the characteristic size of the 7S/C array was set to $0.0256 R_E$, which is the same as that of the flux-rope case, for the gradients of the magnetic field at the barycenter along the trajectory to be obtained.

Only nonzero independent components are displayed, similarly to the flux-rope case. In view of the mathematical expression of the dipole field, 10 independent components of the quadratic gradients and 4 independent components of the linear gradients were nonzero along the crossing path.

Figure 8 shows the variation in the relative errors under iteration at two different points. As shown in Fig. 8a and c, the linear gradients converged to certain values within 60 iterations, with final relative errors of less than 0.02 %. Figure 8b and d show that the quadratic gradients also converge to low errors. After 100 iterations, most of the relative errors in the quadratic gradients were lower than 1 %, and the largest relative error was no more than 6 %. These results suggest that

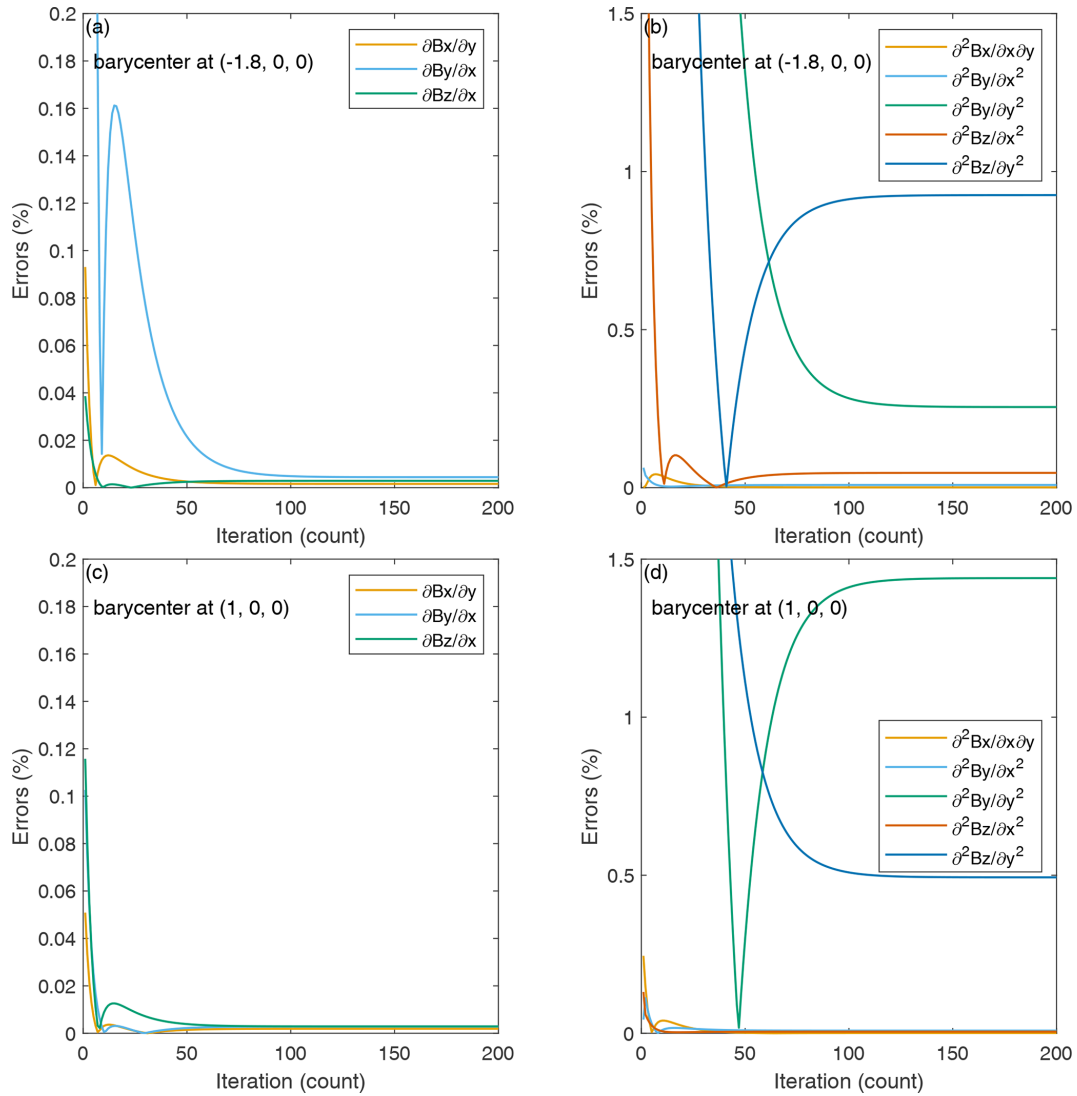


Figure 4. Relative errors in the nonzero components of the linear and quadratic gradients with different iteration numbers at various barycenters.

it is reasonable to set the maximum number of iterations to 100 for the gradients to be derived with good accuracy in this case.

Figure 9 shows a comparison between the nonzero linear gradients derived from our method and those derived from the analytical model. A comparison between the nonzero quadratic gradients derived from the different sources is shown in Fig. 10. Both Figs. 9 and 10 indicate that the algorithm gradients are entirely consistent with those obtained from the accurate model, suggesting that the developed method is effective and precise for use with the dipole field.

Figure 11 shows the relative errors in the gradients at the measured points along the crossing path. All the relative errors for the linear gradients were lower than 0.25 %, and most of the relative errors in the quadratic gradients were lower

than 5 %. It should be noted that the barycenter is at $(2.92, 0, 5) R_E$ at 100 s and the accurate and algorithm quadratic gradient $\nabla_3 \nabla_3 B_3$ is -1.2584 and $-0.6461 \text{ nT } R_E^{-2}$, respectively. The relative error approaches 50 %; however, the absolute error is $0.6123 \text{ nT } R_E^{-2}$, which is approaching zero. The barycenter is at $(-0.04, 0, 5) R_E$ at 63 s and $(0.04, 0, 5) R_E$ at 64 s. Similarly, the absolute errors in the quadratic gradients $\nabla_2 \nabla_2 B_1$ and $\nabla_3 \nabla_3 B_1$ were no more than $1 \text{ nT } R_E^{-2}$, whereas the relative errors were approximately 30 %.

3.3 Discussion

The two analytical magnetic field models (cylindrical force-free flux rope and dipole magnetic field) are simplified and highly symmetrical structures. The linear gradient of the magnetic field has 9 components, while the quadratic gradi-

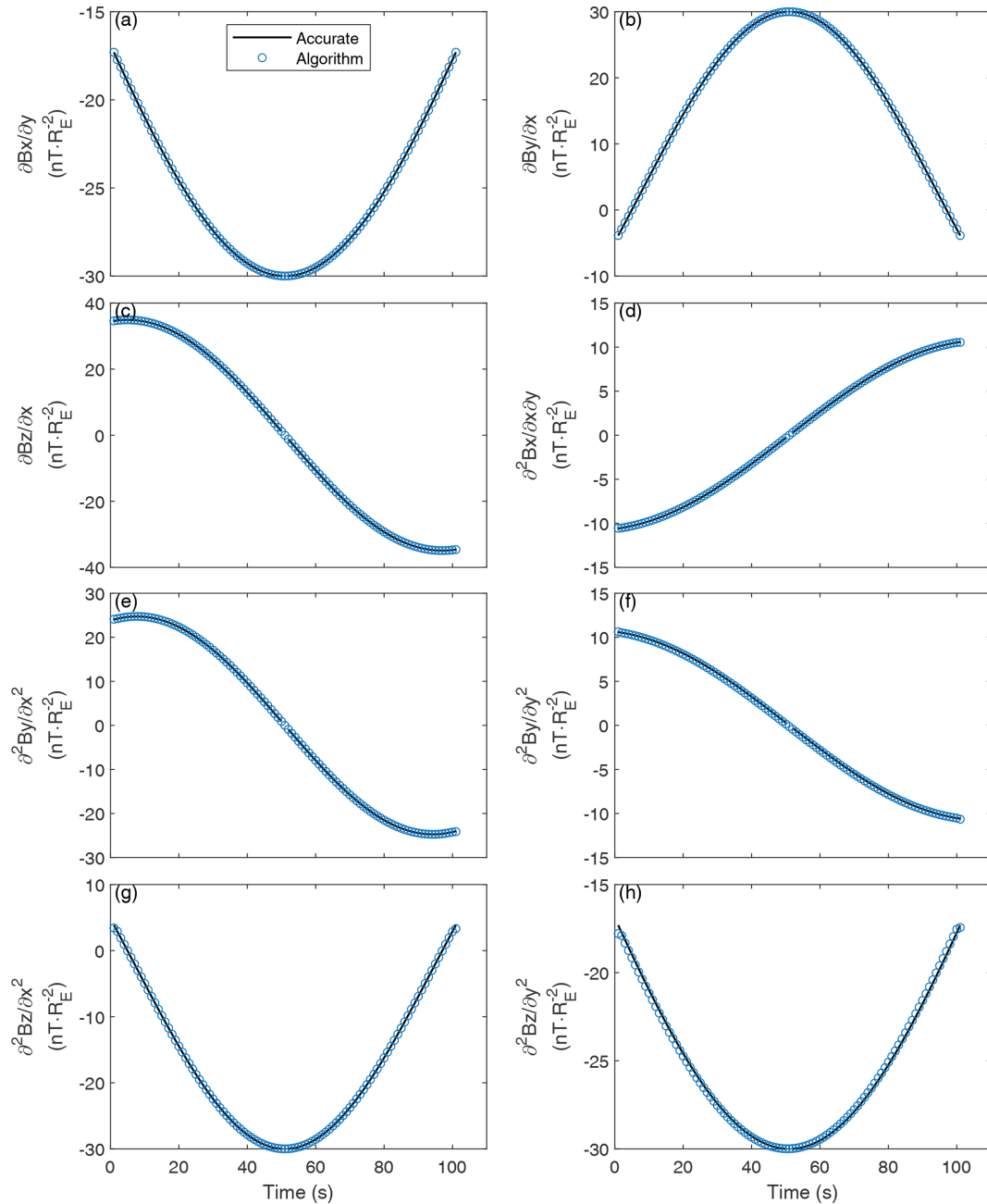


Figure 5. Time series showing nonzero components of the linear and quadratic gradients. Circles and solid lines represent the results obtained using the algorithm and accurate modeling, respectively.

ents comprise 18 independent components due to the symmetry of quadratic gradients. For the flux-rope case, only three components of linear gradient and five components of quadratic gradients have been assessed. But for the dipole-field case, 4 components of linear gradient and 10 components of quadratic gradients have been assessed. The number of assessed parameters has reached half. However, only a subset of the $9 + 18 = 27$ components can be assessed. In this study, we have chosen a symmetric model magnetic field

in order to easily compare our results with the analytic calculations. The zero components of the magnetic gradients are calculated with the algorithm and checked. Further evaluation of the algorithm with a less symmetric magnetosphere model could be useful.

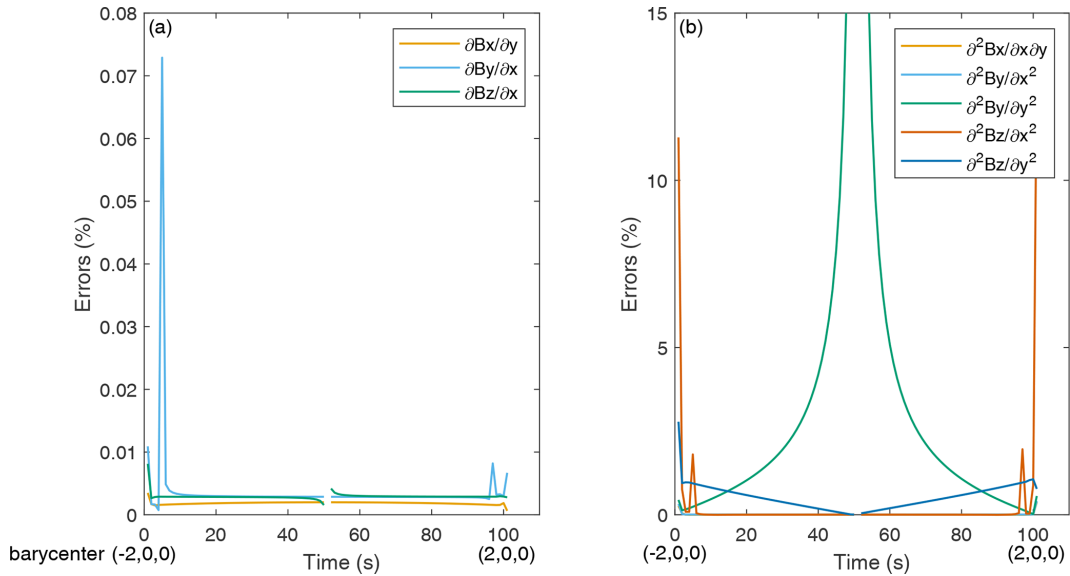


Figure 6. Relative errors in the nonzero components of the linear and quadratic gradients along the crossing path.

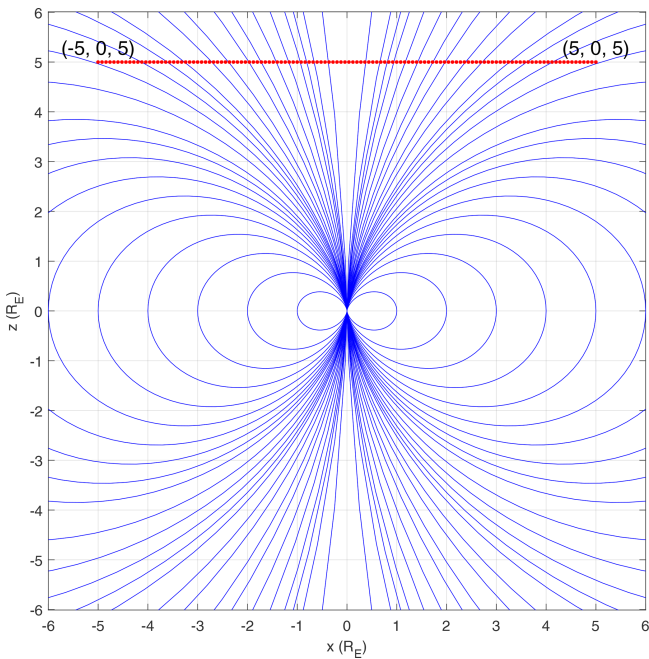


Figure 7. The magnetic dipole field crossed by the 7S/C array. Trajectory of the barycenter of the 7S/C array is from $(-5, 0, 5) R_E$ to $(5, 0, 5) R_E$ over 126 s as shown by the dotted red line. Blue lines represent magnetic field lines.

4 Errors

In this section, we consider the diverse sources of errors – namely, the truncation error, discretization error, iteration error, and measurement error or random error – that can impact the linear and quadratic magnetic spatial gradient estimation.

We introduce and discuss them as follows. Further detailed analyses can be found in Appendices A–D.

Discretization errors arise from the spatial resolution of measurement, which is the combined effect of finite temporal resolution and the relative motion of a probe with respect to the magnetic structure during the measurement period. The significance of these errors can be assessed by comparing the spatial resolution – due to S/C motion during the measurement or the S/C motion in between two successive measurements – with the separation between probes, over which the measured data are subtracted from one another. Typically, spacecraft separation within a constellation ranges from several hundred kilometers to several thousand kilometers, while the temporal resolution of magnetic measurement Δt is about 0.01 s, i.e., $\Delta t = 0.01$ s. Assuming a magnetic structure moves at a velocity of $V < 500 \text{ km s}^{-1}$ relative to the spacecraft, the spatial resolution along the motion direction is about $v\Delta t < 5 \text{ km}$, which is significantly smaller than the S/C separation. Therefore, the corresponding discretization errors are expected to be small.

The iterative method provides converging solutions with decreasing errors as the number of iterations increases as demonstrated in Sect. 3. A particular type of error is the mismatch between the actual limit of the procedure and the approximation reached after a finite number of iterations. This error may be termed the iteration error. We note that it is not associated with the finite resolution of the spacecraft array or the time series. As shown in Fig. 4, the iterative procedures help reduce the calculation error and make the calculation more stable. In addition, once the number of iterations is sufficient (e.g., above 100), the iterative error becomes rather insignificant (see Appendix B).

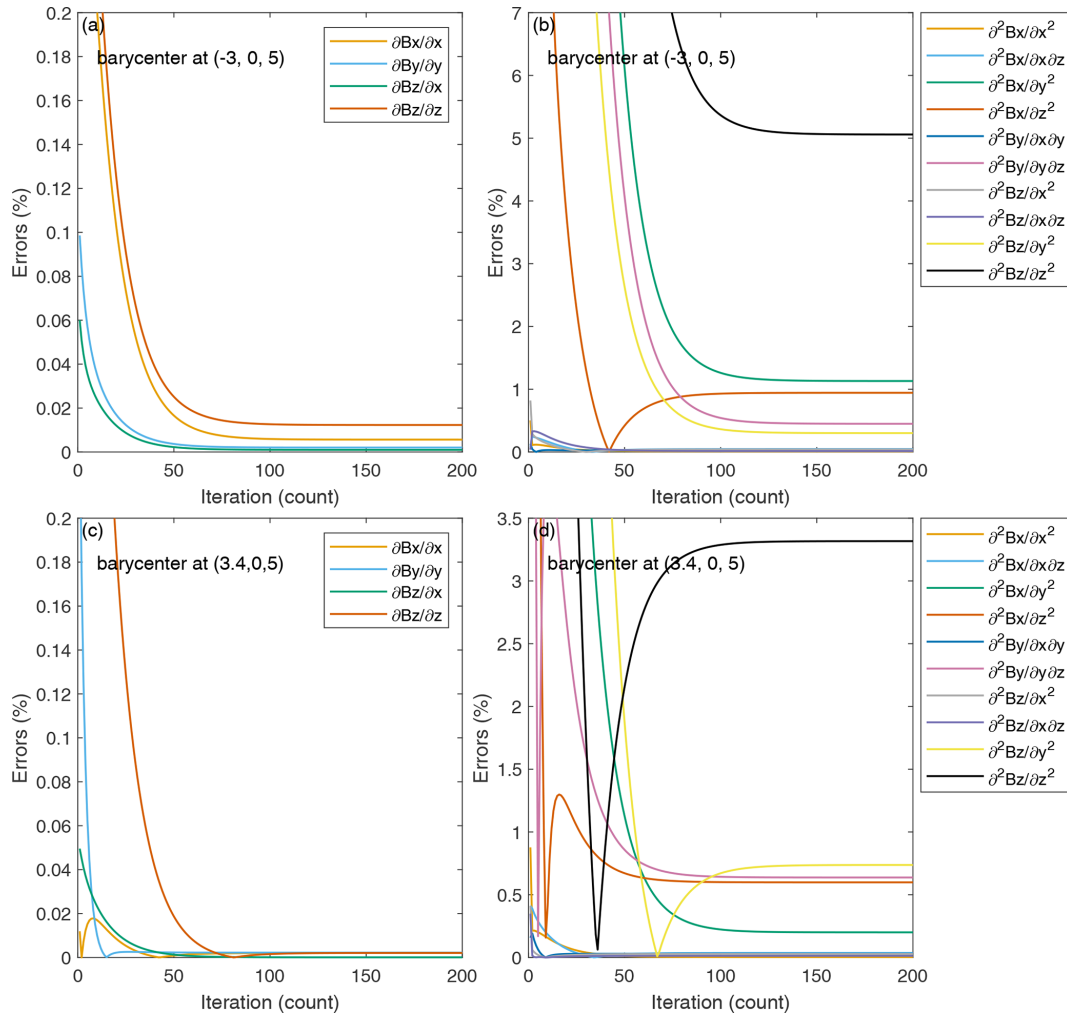


Figure 8. Relative errors in the nonzero components of the linear and quadratic gradients with different iteration numbers at various barycenters.

Due to noise or measurement inaccuracies of input data, the estimated parameters (first and second derivatives) will be subject to random errors. The noise or disturbances in the data can come from the measurement error or the presence of high-frequency (physical) fluctuations, such as those from plasma waves, which can make the calculation of the high-order magnetic gradients very difficult (Shen et al., 2021a). When analyzing the actual observation data, filtering methods should be employed to remove the high-frequency components and avoid the negative effect of the noise. This process would help to extract large-scale magnetic structures under the consideration.

As discussed above, the discretization error and iteration error are expected to be rather small for the magnetic configuration considered. The errors caused by the random measurement errors would be large, and the global features of the magnetic structure would be missed (Shen et al., 2021a). In the following, only the truncation error has been evaluated.

In Sect. 3, the relative error is used to evaluate the truncation error of the proposed method. However, in some cases, evaluation with the relative error is not effective, while the gradient obtained from the accurate model is very small. Furthermore, the truncation error was evaluated under divergence-free magnetic field conditions.

Theoretically, the divergence of the magnetic field and the gradient of the magnetic field divergence are both exactly zero, as shown by $\nabla \cdot \mathbf{B} = 0$ and $|\nabla(\nabla \cdot \mathbf{B})| = 0$. To offer a uniform standard for evaluation, the divergence and gradient of divergence were non-dimensionalized with the corresponding characteristic quantity. The length was calibrated with the spatial characteristic scale of the magnetic structure, D , and the magnetic field was calibrated with the characteristic magnetic field at the barycenter, B_c . Therefore, two evaluation indices were introduced, represented by $(\nabla \cdot \mathbf{B})_c$ and $|\nabla(\nabla \cdot \mathbf{B})_c|$. The values of the two indices can be used to evaluate the accuracies of the linear and quadratic

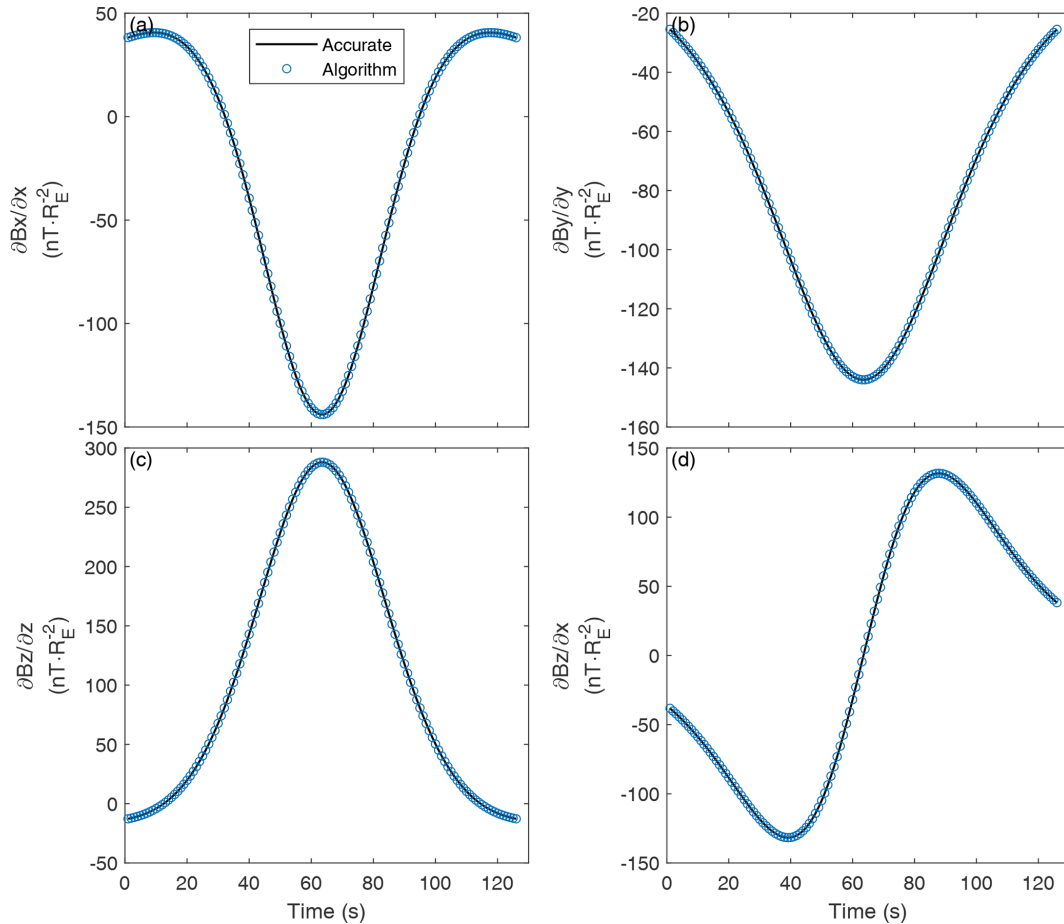


Figure 9. Time series showing nonzero components of the linear gradients. Circles and solid lines represent the results obtained using the algorithm and accurate modeling, respectively.

gradients derived using the proposed method. Nevertheless, this evaluation is not perfect because it cannot include all partial components of the magnetic gradients (the formula $\nabla \cdot \mathbf{B} = 0$ contains 3 of the total of 9 components of $\nabla \mathbf{B}$, while $|\nabla(\nabla \cdot \mathbf{B})| = 0$ contains 9 of the total 18 components of $\nabla \nabla \mathbf{B}$). The advantage of using them as the measures of the errors in the magnetic gradients is that they are robust and simple. We still have not found other, better ways for evaluating the accuracy of the algorithm because the actual values of the magnetic gradients are unknown when analyzing the real observation data.

The algorithm gradients were utilized to calculate the dimensionless divergence and the gradient of divergence for the magnetic field at the barycenter along the crossing path with different characteristic S/C sizes, with the results for the flux-rope and dipole-field cases shown in Figs. 12 and 13, respectively. Figures 12a and 13a show that the dimensionless divergence $(\nabla \cdot \mathbf{B})_c$ at the barycenter is on the order of 10^{-4} , while L varies from 0.0032 to $0.0513 R_E$. The dimensionless gradient of the divergence $|\nabla(\nabla \cdot \mathbf{B})_c|$ for the flux-rope case was lower than 0.02 with $L = 0.0513 R_E$, as shown

in Fig. 12b. Similarly, Fig. 13b shows that $|\nabla(\nabla \cdot \mathbf{B})_c|$ was lower than 0.4, with $L = 0.0513 R_E$, for the dipole field. Meanwhile, $|\nabla(\nabla \cdot \mathbf{B})_c|$ decreased with decreasing L in both cases. These results confirm the accuracy of the proposed method. As evidenced in Figs. 12 and 13, the errors in the first derivative decrease quadratically with the scale L , whereas the errors in the second derivatives decrease linearly with L .

5 Conclusions

In this study, a new algorithm was derived to estimate the linear and quadratic spatial gradients of the magnetic field from simultaneous seven- or nine-point magnetic measurements to obtain the fine structure of the magnetic field and the magnetic field geometry, allowing for the elucidation of whether the seven-spacecraft Plasma Observatory and the nine-spacecraft HelioSwarm missions could be utilized for such measurements. By inputting simultaneous seven–nine-point magnetic measurements and using the reference frame transformation relationships of the magnetic field as well as

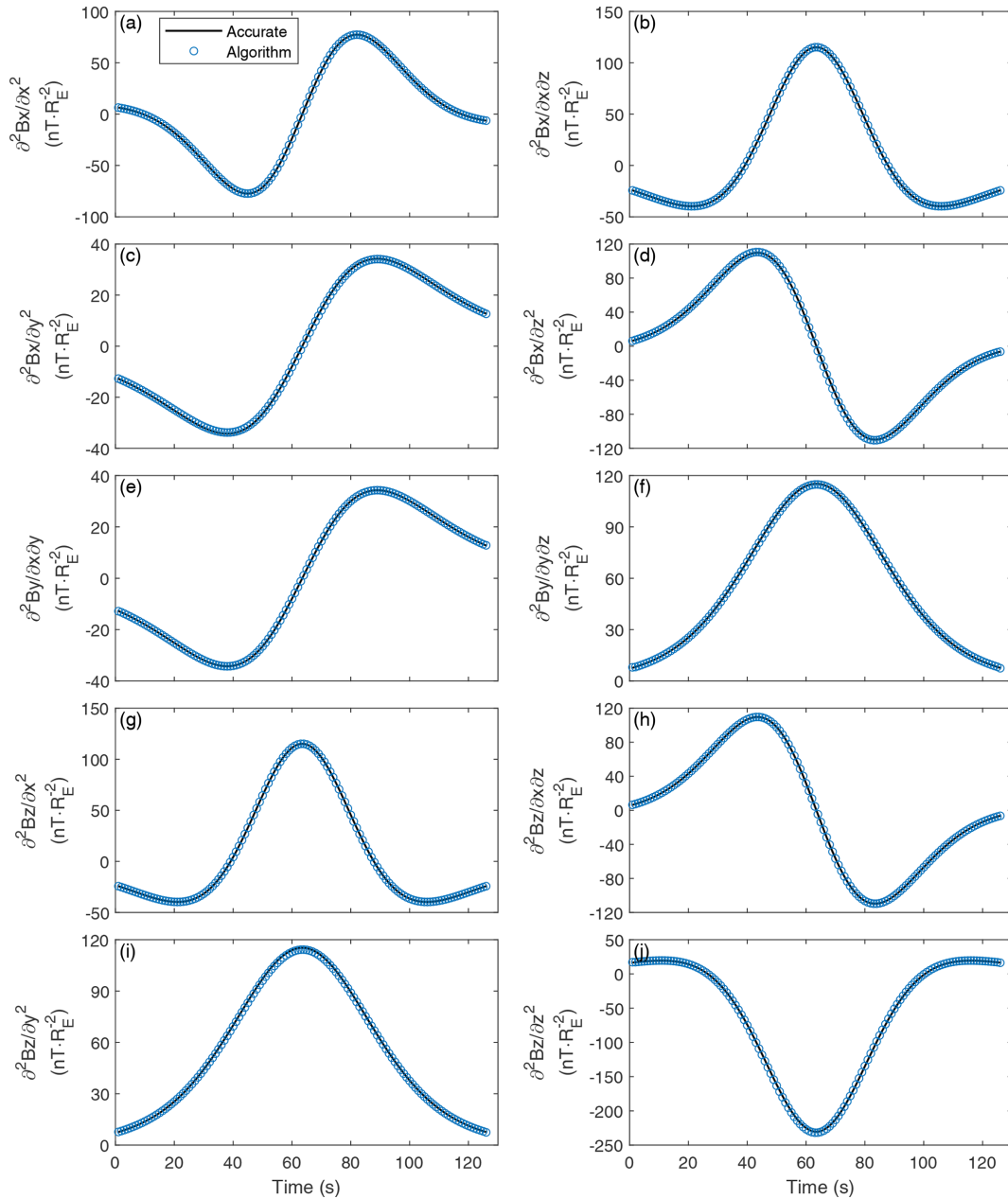


Figure 10. Time series showing nonzero components of the quadratic gradients. Circles and solid lines represent the results obtained using the algorithm and accurate modeling, respectively.

the least-squares method, the new algorithm performs several iterations to finally derive the convergent magnetic linear and quadratic spatial gradients.

The developed algorithm requires only one restriction on the spatial configuration of the constellations, which is that the constellations must be nonplanar. Actual operating constellations can easily satisfy this constraint. Only simultaneous magnetic measurements are required, with no other physical measurements needed, and the only physical constraint of the algorithm is the reference frame transformation

relationship of the magnetic field. In this study, simultaneous magnetic measurements from seven or nine points were assumed to be obtained by identical instruments on board the space mission. Nowadays, the sampling time resolutions of the detectors are already very high, and the temporal variations in the magnetic field or magnetic spatial gradients can be obtained from the time series data. So, this algorithm only focuses on the magnetic spatial gradients, and the magnetic measurements from different spacecraft should be simultaneous. However, the real temporal measurements at different

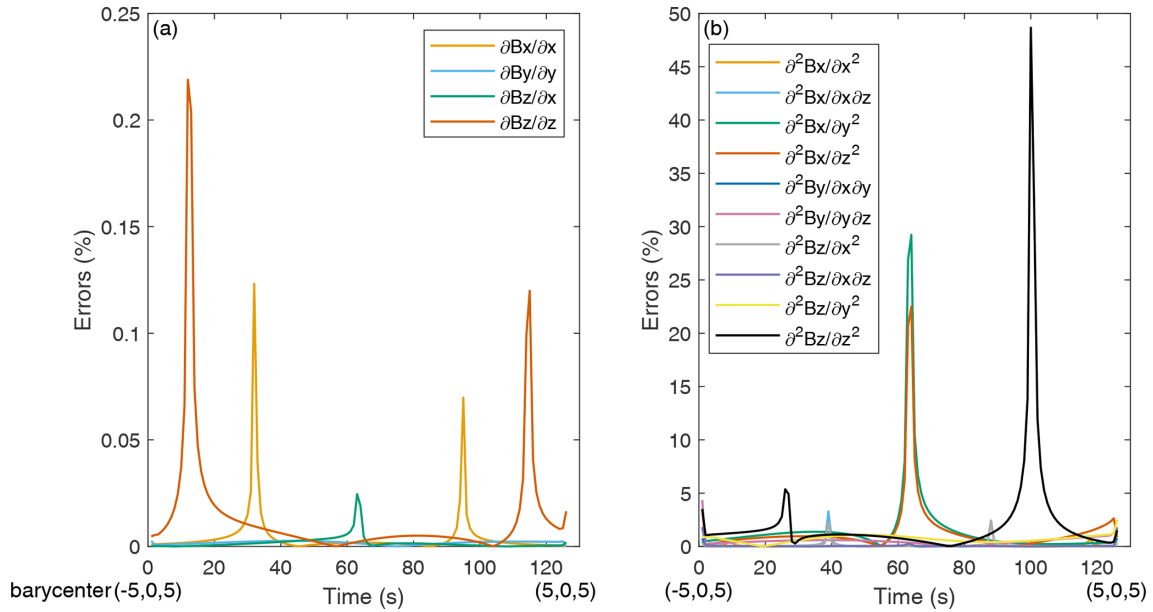


Figure 11. Relative errors in the nonzero components of the linear and quadratic gradients along the crossing path.

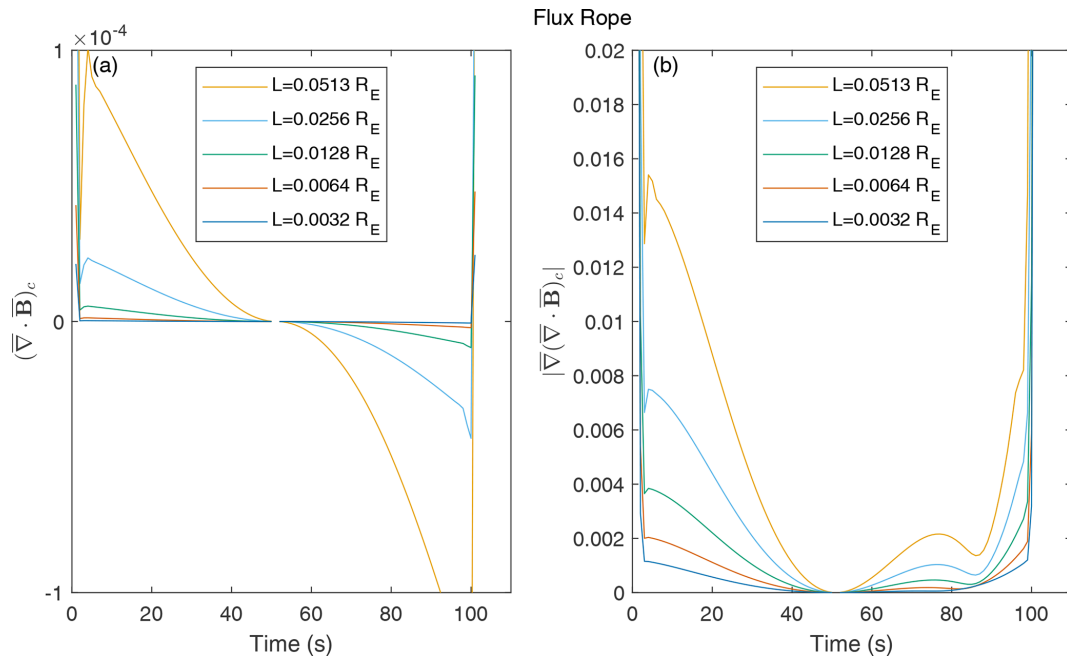


Figure 12. Dimensionless divergence and gradient of divergence for the magnetic field along the flux-rope crossing path with different characteristic S/C sizes (L).

detectors may not be perfectly simultaneous, so the magnetic field data from different detectors need to be synchronized using interpolations. Furthermore, a homogeneous set of instruments on board the constellation may not be achieved, so systematic errors may arise. The total systematic error can be analyzed by the well-established error theory. In this study, the total truncation error has been evaluated. Furthermore, the iteration error, discretization error, and measure-

ment error have been initially evaluated in the Appendix. It is found that the iteration error and discretization error are rather small for the dipole-field case and that the measurement error would cause large error, so the observation data should be filtered during the actual investigations as done in previous research (Shen et al., 2021a). Divergence-free magnetic field conditions were not required to calculate the magnetic spatial gradient. Alternatively, in the algorithm,

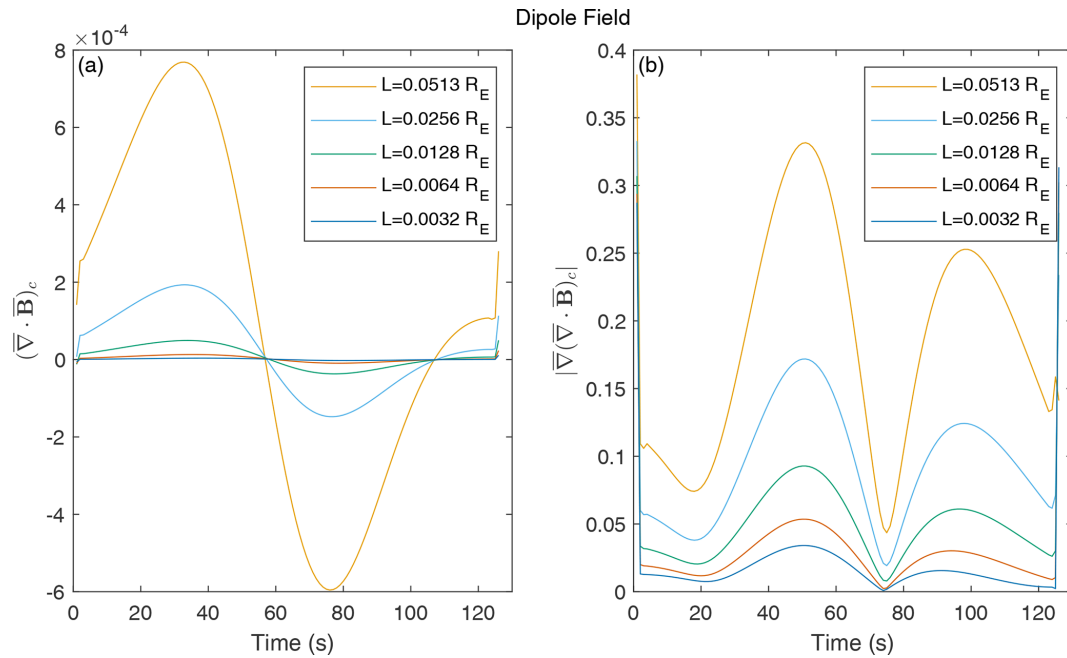


Figure 13. Dimensionless divergence and gradient of divergence for the magnetic field along the dipole-field crossing path with different characteristic S/C sizes (L).

the magnitudes of the magnetic divergence and its gradient were used to evaluate the truncation errors in the linear and quadratic magnetic spatial gradients, respectively.

The proposed algorithm was verified using a cylindrical force-free flux rope and a dipole magnetic field, with results showing that the iterations effectively converged and that the magnetic spatial gradients can reach reasonable accuracy. The results of this study can thus be applied to the analysis of magnetic field data from multi-spacecraft constellations (e.g., the Plasma Observatory and HelioSwarm) and to the design of future constellation missions.

Appendix A: Truncation error

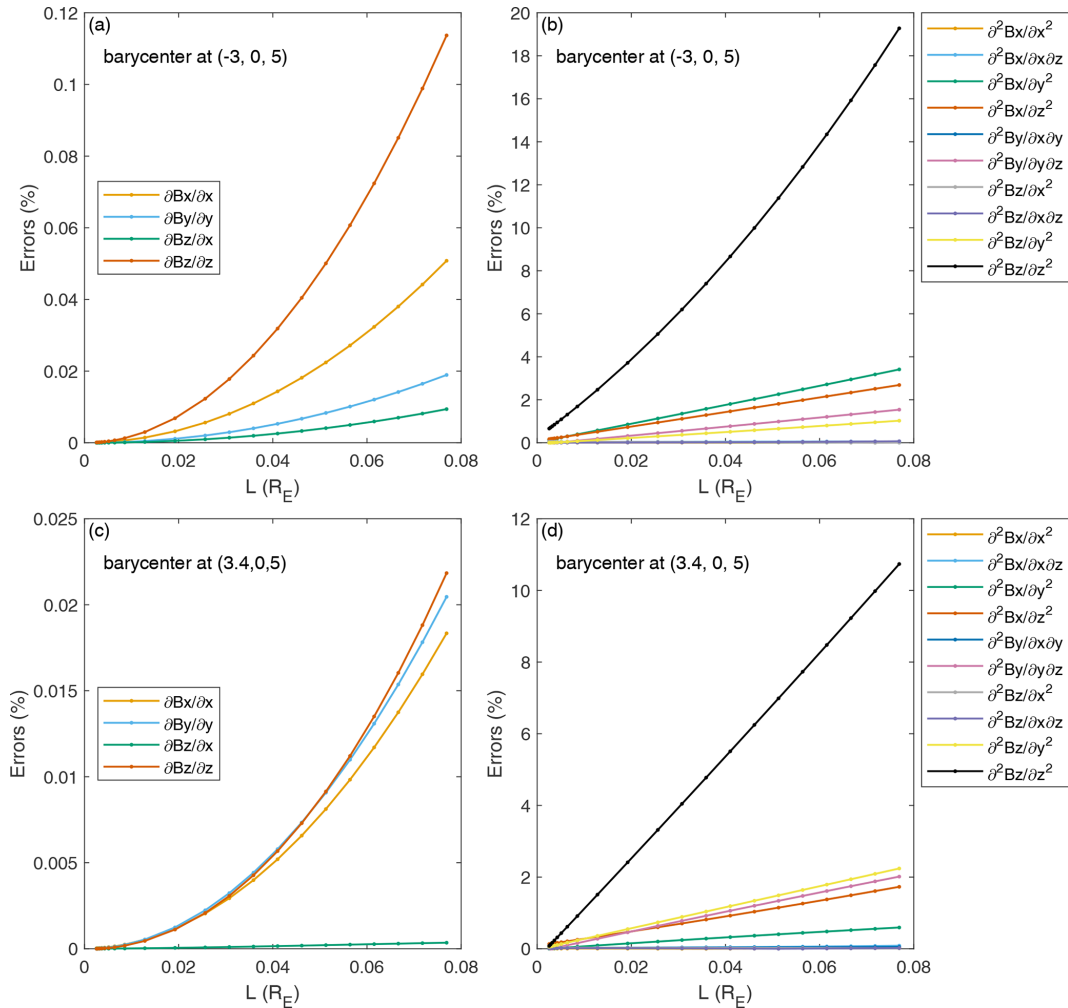


Figure A1. The total relative errors in the nonzero components of the linear and quadratic gradients with different characteristic size (L) at various barycenter positions for the dipole-field case.

In the following error analysis, only the dipole-field case is taken as an example. In Sect. 4, the dimensionless divergence and gradient of the divergence of the magnetic field have been used as the measures of the errors in the first-order and second-order magnetic gradients, respectively. And Fig. 13 shows the dimensionless divergence and gradient of the divergence with various characteristic S/C sizes. Nevertheless, the divergence and gradient of the divergence do not contain all the components of the magnetic gradients. In Appendix A, the truncation errors in the nonzero and independent components of the first-order and second-order magnetic gradients have been investigated, respectively. The truncation error is evaluated by the total relative error, which has been defined as $|(X_{\text{algorithm}} - X_{\text{accurate}})/X_{\text{accurate}}| \times 100\%$ in Sect. 3.1. Figure A1 shows the total relative errors in the nonzero components of the linear and quadratic gradients with a different characteristic size (L). As evidenced in Fig. A1, the

truncation error decreases as the distance between satellites is reduced. Furthermore, the errors in the first derivative decrease quadratically as the scale L is reduced, whereas the errors in the second derivatives decrease linearly with L reducing.

Appendix B: Iteration error

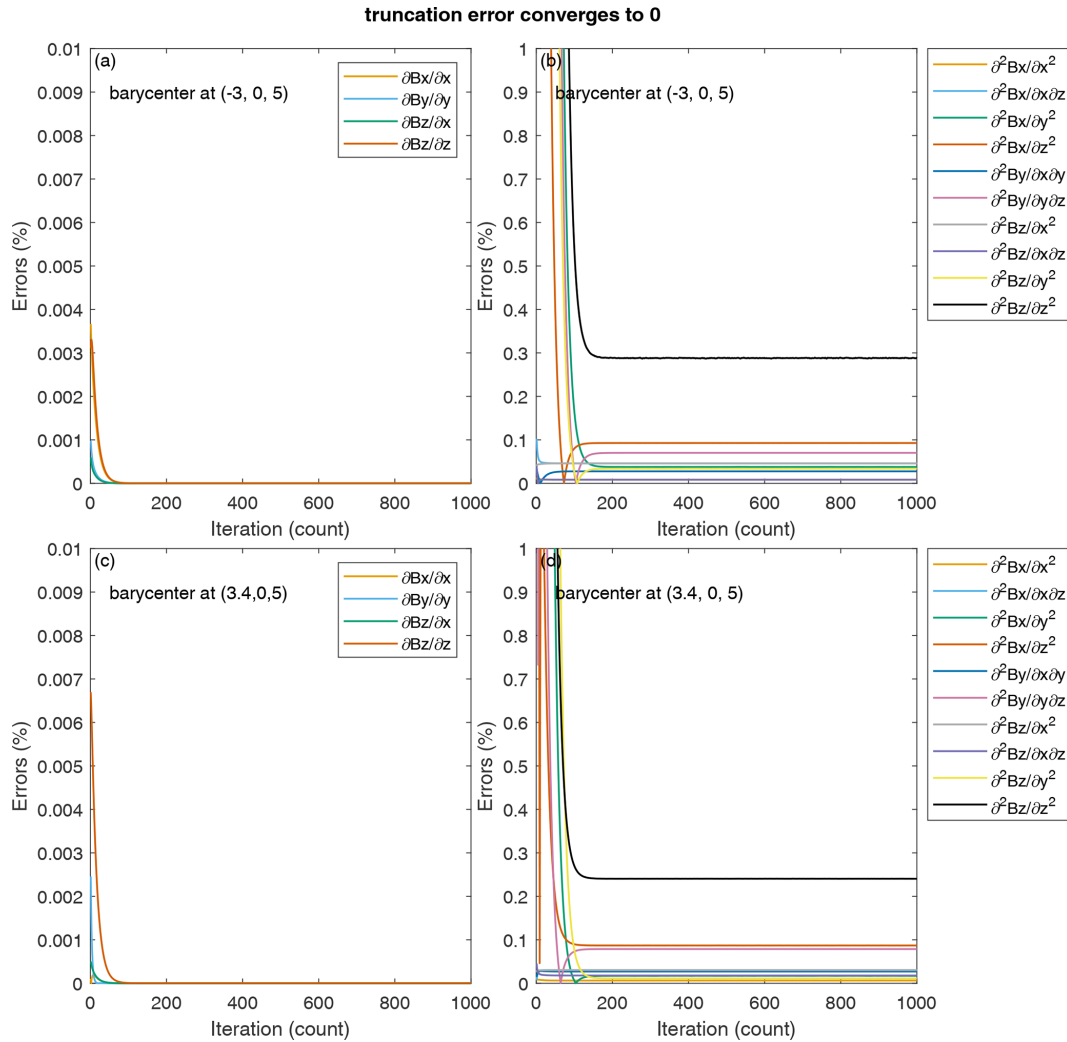


Figure B1. As the truncation error converges to zero, these are the total relative errors in the nonzero components of the linear and quadratic gradients with different iteration numbers at various barycenters for the dipole-field case.

By holding the configuration of the 7S/C constellation, the distances between satellites are scaled down by a factor of 100, which decreases the characteristic size of the 7S/C array to $L = 0.2564 \times 10^{-3} R_E$. Due to this reduction, the high-order truncation error converges to zero. In Sect. 3.2, the cut-off number of iterations was set to 100. In order to clearly show the convergence of the iterations, the number of iterations was increased to 1000. Figure B1 shows the variation in the total relative errors in the linear and quadratic gradients with respect to the iteration numbers for the dipole-field case. The total relative errors in the four nonzero components of linear gradients at point $(-3, 0, 5)$ and $(3.4, 0, 5)$ are both lower than $10^{-6} \%$. The total relative errors in the 10 nonzero components of quadratic gradients at point $(-3, 0, 5)$ are 0.0085 %, 0.0459 %, 0.0377 %, 0.0928 %, 0.0276 %, 0.0701 %, 0.0459 %, 0.0083 %, 0.0338 %, and

0.2880 %, while those at point $(3.4, 0, 5)$ are 0.0063 %, 0.0304 %, 0.0171 %, 0.0870 %, 0.0271 %, 0.0788 %, 0.0304 %, 0.0180 %, 0.0112 %, and 0.2405 %, respectively. It is found that the total relative errors in the linear gradients decrease to 0 and those of the majority quadratic gradients decrease to less than 0.1 %, with the distances between satellites reduced. The iteration error goes to zero asymptotically.

Appendix C: Discretization error

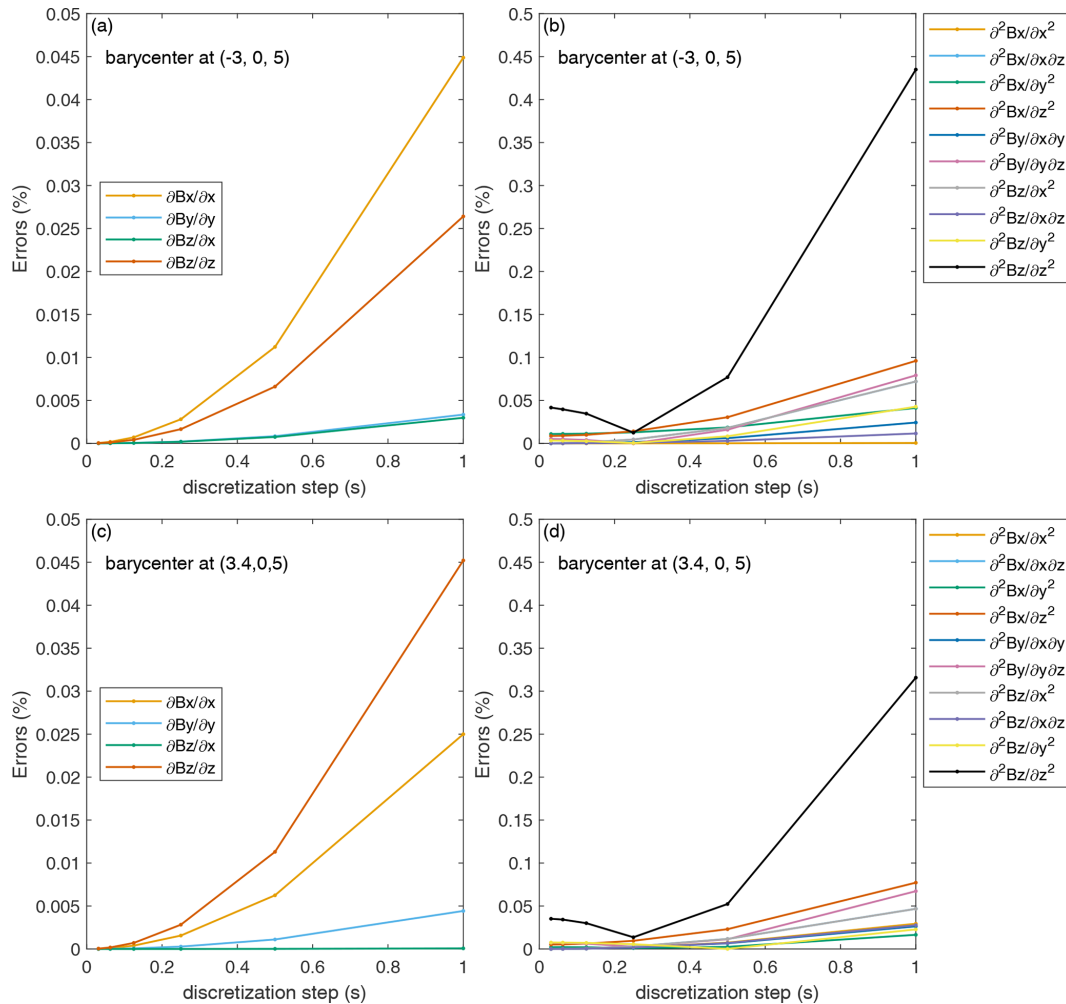


Figure C1. As the truncation error converges to zero, these are the total relative errors in the linear and quadratic gradients with different discretization steps at various barycenters for the dipole-field case, with a discretization error introduced.

In Sect. 3, the magnetic field measurement is instantaneous, and the resolution of measurement is set to 1 s. It is assumed that the magnetic field value at the measurement point is the average along the satellite's trajectory for a duration of 0.5 s before and after the point in the direction of the satellite's motion. This assumption introduces a discretization error, and the discretization step is defined as 1 s accordingly. The characteristic size of the 7S/C array is decreased to $L = 0.2564 \times 10^{-3} R_E$. So, the truncation error converges to zero, leaving only the discretization error. If the resolution of the magnetic field measurement changes to 0.5 s, the duration time before and after the measurement point is set to 0.25 s accordingly. And the discretization step is reduced to 0.5 s. Figure C1 shows the variation in total relative errors in the linear and quadratic gradients with respect to the discretization steps for the dipole-field case, with a discretization error introduced. The total relative errors in the 4 nonzero

components of linear gradients are no higher than 0.05 %, while the total relative errors in the 10 nonzero components of quadratic gradients are no higher than 0.5 %. The truncation error is decreased as the discretization step is reduced. It can be suggested that the discretization error is relatively small.

Appendix D: Measurement error

In order to evaluate the measurement error, the random Gaussian errors with a mean of 0 and a standard deviation of 0.01 are imposed on the magnetic field measurements. The results show that the total relative errors in linear gradients are about 1 %. However, the total relative errors in the majority of quadratic gradients are higher than 10 %, and individual errors even exceed 100 %. This algorithm would

represent negative robustness to measurement noise. Shen et al. (2021a) have developed a novel algorithm that can estimate the quadratic magnetic gradient from multi-spacecraft measurements. This novel algorithm has been verified to be effective in analyzing MMS (Magnetospheric Multiscale mission) observations. In their investigation, the magnetic field data have to be filtered by a low-pass filter to eliminate disturbances; otherwise, the errors caused by these disturbances would be very large. It can be suggested that the observation data should be filtered to remove noise when applying our algorithm.

Code availability. The code for calculating the linear and quadratic magnetic gradients is available in the Supplement.

Data availability. The data in this study are generated by formulas or our algorithm. Further information is available upon request.

Supplement. The supplement related to this article is available online at: <https://doi.org/10.5194/angeo-43-115-2025-supplement>.

Author contributions. CS designed the method, and RK gave some advice. GZ developed the model code and performed the test. CS and GZ wrote the paper. CS and RK reviewed and edited the paper. YZ helped to evaluate the method.

Competing interests. The contact author has declared that none of the authors has any competing interests.

Disclaimer. Publisher's note: Copernicus Publications remains neutral with regard to jurisdictional claims made in the text, published maps, institutional affiliations, or any other geographical representation in this paper. While Copernicus Publications makes every effort to include appropriate place names, the final responsibility lies with the authors.

Acknowledgements. Work at IRAP was supported by the National Centre for Scientific Research (CNRS), the French National Space Agency (CNES), and the University of Toulouse (UPS). RK acknowledges the postdoctoral fellowship from CNES.

Financial support. This work was supported by the National Natural Science Foundation of China (grant no. 42130202), National Key Research and Development Program of China (grant no. 2022YFA1604600), and Hubei Provincial Natural Science Foundation of China (grant no. 2022CFB928). This research was also supported by the Shenzhen Technology Project (grant no. JCYJ20241202123905008) and the International Space Science In-

stitute (ISSI) in Bern through the ISSI International Team project no. 556 (cross-scale energy transfer in space plasmas).

Review statement. This paper was edited by Oliver Allanson and reviewed by Johan De Keyser and one anonymous referee.

References

- Broeren, T., Klein, K. G., TenBarge, J. M., Dors, I., Roberts, O. W., and Verscharen, D.: Magnetic Field Reconstruction for a Realistic Multi-Point, Multi-Scale Spacecraft Observatory, *Front. Astron. Space Sci.*, 8, 727076, <https://doi.org/10.3389/fspas.2021.727076>, 2021.
- Burch, J. L. and Phan, T. D.: Magnetic reconnection at the dayside magnetopause: Advances with MMS, *Geophys. Res. Lett.*, 43, 8327–8338, <https://doi.org/10.1002/2016GL069787>, 2016.
- Burch, J. L., Moore, T. E., Torbert, R. B., and Giles, B. L.: Magnetospheric multiscale overview and science objectives, *Space Sci. Rev.*, 199, 5–21, <https://doi.org/10.1007/s11214-015-0164-9>, 2015.
- Chanteur, G.: Spatial Interpolation for four spacecraft: Theory, in: Analysis methods for multi-spacecraft data, edited by: Paschmann, G. and Daly, P. W., European Space Agency Publ. Division, Noordwijk, the Netherlands, 349–370, ISBN 1608-280X, 1998.
- Chanteur, G. and Harvey, C. C.: Spatial interpolation for four spacecraft: Application to magnetic gradients, in: Analysis methods for multi-spacecraft data, edited by: Paschmann, G. and Daly, P. W., European Space Agency Publications Division, Noordwijk, the Netherlands, 371–394, ISBN 1608-280X, 1998.
- Chian, A. C. L., Borotto, F. A., and Gonzalez, W. D.: Alfvén Intermittent Turbulence Driven by Temporal Chaos, *Astrophys. J.*, 505, 993, <https://doi.org/10.1086/306214>, 1998.
- Chian, A. C. L., Borotto, F. A., Hada, T., Miranda, R. A., Muñoz, P. R., and Rempel, E. L.: Nonlinear dynamics in space plasma turbulence: Temporal stochastic chaos, *Rev. Mod. Plasma Phys.*, 6, 34, <https://doi.org/10.1007/s41614-022-00095-z>, 2022.
- De Keyser, J.: Least-squares multi-spacecraft gradient calculation with automatic error estimation, *Ann. Geophys.*, 26, 3295–3316, <https://doi.org/10.5194/angeo-26-3295-2008>, 2008.
- De Keyser, J., Darrouzet, F., Dunlop, M. W., and Décréau, P. M. E.: Least-squares gradient calculation from multi-point observations of scalar and vector fields: methodology and applications with Cluster in the plasmasphere, *Ann. Geophys.*, 25, 971–987, <https://doi.org/10.5194/angeo-25-971-2007>, 2007.
- Denton, R. E., Torbert, R. B., Hasegawa, H., Dors, I., Genestreti, K. J., Argall, M. R., Gershman, D., Le Contel, O., Burch, J. L., Russell, C. T., Strangeway, R. J., Giles, B. L., and Fischer, D.: Polynomial reconstruction of the reconnection magnetic field observed by multiple spacecraft, *J. Geophys. Res.-Space*, 125, e2019JA027481, <https://doi.org/10.1029/2019JA027481>, 2020.
- Dong, X.-C., Dunlop, M. W., Wang, T.-Y., Cao, J.-B., Trattner, K. J., Bamford, R., Russell, C. T., Bingham, R., Strangeway, R. J., Fear, R. C., Giles, B. L., and Torbert, R. B.: Carriers and sources of magnetopause current: MMS case study, *J. Geophys. Res.-Space*, 123, 5464–5475, <https://doi.org/10.1029/2018JA025292>, 2018.

- Dunlop, M. W., Balogh, A., and Glassmeier, K.-H.: Four-point Cluster application of magnetic field analysis tools: The discontinuity analyzer, *J. Geophys. Res.*, 107, 1385, <https://doi.org/10.1029/2001JA005089>, 2002a.
- Dunlop, M. W., Balogh, A., Glassmeier, K.-H., and Robert, P.: Four-point cluster application of magnetic field analysis tools: The curlometer, *J. Geophys. Res.*, 107, 1384, <https://doi.org/10.1029/2001JA005088>, 2002b.
- Escoubet, C. P., Schmidt, R., and Goldstein, M. L.: Cluster–Science and mission overview, *Space Sci. Rev.*, 79, 11–32, <https://doi.org/10.1023/A:1004923124586>, 1997.
- Escoubet, C. P., Fehringer, M., and Goldstein, M.: *Introduction* The Cluster mission, *Ann. Geophys.*, 19, 1197–1200, <https://doi.org/10.5194/angeo-19-1197-2001>, 2001.
- Haaland, S., Hasegawa, H., Paschmann, G., Sonnerup, B., and Dunlop, M.: 20 years of Cluster observations: The magnetopause, *J. Geophys. Res.*, 126, JA029362, e2021, <https://doi.org/10.1029/2021JA029362>, 2021.
- Hamrin, M., Rönmark, K., Börlin, N., Vedin, J., and Vaivads, A.: GALS – Gradient Analysis by Least Squares, *Ann. Geophys.*, 26, 3491–3499, <https://doi.org/10.5194/angeo-26-3491-2008>, 2008.
- Harvey, C. C.: Spatial gradients and the volumetric tensor, in: *Analysis methods for multi-spacecraft data*, edited by: Paschmann, G. and Daly, P. W., European Space Agency Publ. Division, Noordwijk, the Netherlands, 307–322, ISBN 1608-280X, 1998.
- Kieokaew, R., Foullon, C., and Lavraud, B.: Four-Spacecraft Magnetic Curvature and Vorticity Analyses on Kelvin-Helmholtz Waves in MHD Simulations, *J. Geophys. Res.*, 123, 513–529, <https://doi.org/10.1002/2017JA024424>, 2018.
- Kieokaew, R. and Foullon, C.: Kelvin-Helmholtz Waves Magnetic Curvature and Vorticity: Four-Spacecraft Cluster Observations, *J. Geophys. Res.*, 124, 3347–3359, <https://doi.org/10.1029/2019JA026484>, 2019.
- Klein, K. G., Spence, H., Alexandrova, O., Argall, M., Arzamasov, L., Bookbinder, J., Broeren, T., Caprioli, D., Case, A., Chandran, B., Chen, L.-J., Dors, I., Eastwood, J., Forsyth, C., Galvin, A., Genot, V., Halekas, J., Hesse, M., Hine, B., Horbury, T., Jian, L., Kasper, J., Kretzschmar, M., Kunz, M., Lavraud, B., Le Contel, O., Mallet, A., Maruca, B., Matthaeus, W., Niehof, J., O’Brien, H., Owen, C., Retinò, A., Reynolds, C., Roberts, O., Schekochihin, A., Skoug, R., Smith, C., Smith, S., Steinberg, J., Stevens, M., Szabo, A., TenBarge, J., Torbert, R., Vasquez, B., Verscharen, D., Whittlesey, P., Wickizer, B., Zank, G., and Zweibel, E.: HelioSwarm: A Multipoint, Multi-scale Mission to Characterize Turbulence, *Space Sci. Rev.*, 219, 74, <https://doi.org/10.1007/s11214-023-01019-0>, 2023.
- Liu, Y. Y., Fu, H. S., Olshevsky, V., Pontin, D. I., Liu, C. M., Wang, Z., Chen, G., Dai, L., and Retino, A.: SOTE: A non-linear method for magnetic topology reconstruction in space plasmas, *Astrophys. J.*, 244, 31, <https://doi.org/10.3847/1538-4365/ab391a>, 2019.
- Lundquist, S.: Magnetohydrostatic fields, *Ark. Fys.*, 2, 361–365, 1950.
- Pecora, F., Yang, Y., Matthaeus, W. H., Chasapis, A., Klein, K. G., Stevens, M., Servidio, S., Greco, A., Gershman, D. J., Giles, B. L., and Burch, J. L.: Three-Dimensional Energy Transfer in Space Plasma Turbulence from Multipoint Measurement, *Phys. Rev. Lett.*, 131, 225201, <https://doi.org/10.1103/PhysRevLett.131.225201>, 2023.
- Pitout, F. and Bogdanova, Y. V.: The polar cusp seen by Cluster, *J. Geophys. Res.*, 126, JA029582, <https://doi.org/10.1029/2021JA029582>, 2021.
- Politano, H. and Pouquet, A.: Von Kármán–Howarth equation for magnetohydrodynamics and its consequences on third-order longitudinal structure and correlation functions, *Phys. Rev. E.*, 57, R21–R24, <https://doi.org/10.1103/PhysRevE.57.R21>, 1998a.
- Politano, H. and Pouquet, A.: Dynamical length scales for turbulent magnetized flows, *Geophys. Res. Lett.*, 25, 273–276, <https://doi.org/10.1029/97GL03642>, 1998b.
- Retinò, A., Khotyaintsev, Y., Le Contel, O., Marcucci, M. F., Plaschke, F., Vaivads, A., Angelopoulos, V., Blasi, P., Burch, J., De Keyser, J., Dunlop, M., Dai, L., Eastwood, J., Fu, H., Haaland, S., Hoshino, M., Johlander, A., Kepko, L., Kucharek, H., Lapenta, G., Lavraud, B., Mandraki, O., Matthaeus, W., McWilliams, K., Petrukovich, A., Pinçon, J.-L., Saito, Y., Sorriso-Valvo, L., Vainio, R., and Wimmer-Schweingruber, R.: Particle energization in space plasmas: towards a multi-point, multi-scale plasma observatory, *Exp. Astron.*, 54, 427–471, <https://doi.org/10.1007/s10686-021-09797-7>, 2022.
- Robert, P., Roux, A., Harvey, C. C., Dunlop, M. W., Daly, P. W., and Glassmeier, K.-H.: Tetrahedron geometric factors, in: *Analysis methods for multi-spacecraft data*, edited by: Paschmann, G. and Daly, P. W., European Space Agency Publ. Division, Noordwijk, the Netherlands, 323–348, ISBN 1608-280X, 1998.
- Rong, Z. J., Wan, W. X., Shen, C., Li, X., Dunlop, M. W., Petrukovich, A. A., Zhang, T. L., and Lucek, E.: Statistical survey on the magnetic structure in magnetotail current sheets, *J. Geophys. Res.*, 116, A09218, <https://doi.org/10.1029/2011JA016489>, 2011.
- Runov, A., Sergeev, V. A., Nakamura, R., Baumjohann, W., Apatenkov, S., Asano, Y., Takada, T., Volwerk, M., Vörös, Z., Zhang, T. L., Sauvaud, J.-A., Rème, H., and Balogh, A.: Local structure of the magnetotail current sheet: 2001 Cluster observations, *Ann. Geophys.*, 24, 247–262, <https://doi.org/10.5194/angeo-24-247-2006>, 2006.
- Russell, C. T., Mellott, M. M., Smith, E. J., and King, J. H.: Multiple spacecraft observations of interplanetary shocks: Four spacecraft determination of shock normals, *J. Geophys. Res.*, 88, 4739–4748, <https://doi.org/10.1029/JA088iA06p04739>, 1983.
- Shen, C., Li, X., Dunlop, M., Liu, Z. X., Balogh, A., Baker, D. N., Hapgood, M., and Wang, X.: Analyses on the geometrical structure of magnetic field in the current sheet based on cluster measurements, *J. Geophys. Res.*, 108, 1168, <https://doi.org/10.1029/2002JA009612>, 2003.
- Shen, C., Liu, Z. X., Li, X., Dunlop, M., Lucek, E., Rong, Z. J., Chen, Z. Q., Escoubet, C. P., Malova, H. V., Lui, A. T. Y., Fazakerley, A., Walsh, A. P., and Mouikis, C.: Flattened current sheet and its evolution in substorms, *J. Geophys. Res.*, 113, A07S21, <https://doi.org/10.1029/2007JA012812>, 2008.
- Shen, C., Rong, Z. J., Dunlop, M. W., Ma, Y. H., Li, X., Zeng, G., Yan, G. Q., Wan, W. X., Liu, Z. X., Carr, C. M., and Rème, H.: Spatial gradients from irregular, multipoint spacecraft configurations, *J. Geophys. Res.*, 117, A11207, <https://doi.org/10.1029/2012JA018075>, 2012.
- Shen, C., Yang, Y. Y., Rong, Z. J., Li, X., Dunlop, M., Carr, C. M., Liu, Z. X., Baker, D. N., Chen, Z. Q., Ji, Y., and Zeng, G.: Direct calculation of the ring current distribution and magnetic structure

- seen by Cluster during geomagnetic storms, *J. Geophys. Res.*, 119, 2458–2465, <https://doi.org/10.1002/2013JA019460>, 2014.
- Shen, C., Zeng, G., Zhang, C., Rong, Z., Dunlop, M., Russell, C. T., Escoubet, C. P., and Ren, N.: Determination of the configurations of boundaries in space, *J. Geophys. Res.*, 125, JA028163, <https://doi.org/10.1029/2020JA028163>, 2020.
- Shen, C., Zhang, C., Rong, Z., Pu, Z., Dunlop, M. W., Escoubet, C. P., Russell, C. T., Zeng, G., Ren, N., Burch, J. L., and Zhou, Y.: Nonlinear magnetic gradients and complete magnetic geometry from multispacecraft measurements, *J. Geophys. Res.*, 126, JA028846, <https://doi.org/10.1029/2020JA028846>, 2021a.
- Shen, C., Zhou, Y. F., Ma, Y. H., Wang, X. G., Pu, Z. Y., and Dunlop, M.: A general algorithm for the linear and quadratic gradients of physical quantities based on 10 or more point measurements, *J. Geophys. Res.*, 126, JA029121, <https://doi.org/10.1029/2021JA029121>, 2021b.
- Shi, J. K., Cheng, Z. W., Zhang, T. L., Dunlop, M., Liu, Z. X., Torkar, K., Fazakerley, A., Lucek, E., Rème, H., Dandouras, I., Lui, A. T. Y., Pu, Z. Y., Walsh, A. P., Volwerk, M., Lahiff, A. D., Taylor, M. G. G. T., Grocott, A., Kistler, L. M., Lester, M., Moukikis, C., and Shen, C.: South-north asymmetry of field-aligned currents in the magnetotail observed by Cluster, *J. Geophys. Res.*, 115, A07228, <https://doi.org/10.1029/2009JA014446>, 2010.
- Shi, Q. Q., Shen, C., Pu, Z. Y., Dunlop, M. W., Zong, Q. G., Zhang, H., Xiao, C. J., Liu, Z. X., and Balogh, A.: Dimensional analysis of observed structures using multipoint magnetic field measurements: Application to Cluster, *Geophys. Res. Lett.*, 32, L12105, <https://doi.org/10.1029/2005GL022454>, 2005.
- Sonnerup, B. U. Ö., Haaland, S., Paschmann, G., Lavraud, B., Dunlop, M. W., Rème, H., and Balogh, A.: Orientation and motion of a discontinuity from single-spacecraft measurements of plasma velocity and density: Minimum mass flux residue, *J. Geophys. Res.*, 109, A03221, <https://doi.org/10.1029/2003JA010230>, 2004.
- Torbert, R. B., Dors, I., Argall, M. R., Genestreti, K. J., Burch, J. L., Farrugia, C. J., Forbes, T. G., Giles, B. L., and Strangeway, R. J.: A new method of 3-D magnetic field reconstruction, *Geophys. Res. Lett.*, 47, GL085542, <https://doi.org/10.1029/2019GL085542>, 2020.
- Vogt, J., Albert, A., and Marghitu, O.: Analysis of three-spacecraft data using planar reciprocal vectors: methodological framework and spatial gradient estimation, *Ann. Geophys.*, 27, 3249–3273, <https://doi.org/10.5194/angeo-27-3249-2009>, 2009.
- Vogt, J., Sorbalo, E., He, M., and Blagau, A.: Gradient estimation using configurations of two or three spacecraft, *Ann. Geophys.*, 31, 1913–1927, <https://doi.org/10.5194/angeo-31-1913-2013>, 2013.
- Yang, Y.: Energy Transfer and Dissipation in Plasma Turbulence: From Compressible MHD to Collisionless Plasma, Springer Theses, Springer Singapore, <https://doi.org/10.1007/978-981-13-8149-2>, 2019.
- Zhang, Q.-H., Dunlop, M. W., Lockwood, M., Holme, R., Kamide, Y., Baumjohann, W., Liu, R.-Y., Yang, H.-G., Woodfield, E. E., Hu, H.-Q., Zhang, B.-C., and Liu, S.-L.: The distribution of the ring current: Cluster observations, *Ann. Geophys.*, 29, 1655–1662, <https://doi.org/10.5194/angeo-29-1655-2011>, 2011.
- Zhou, Y. and Shen, C.: Estimating gradients of physical fields in space, *Ann. Geophys.*, 42, 17–28, <https://doi.org/10.5194/angeo-42-17-2024>, 2024.